Energy & Environmental Science

ROYAL SOCIETY OF CHEMISTRY

REVIEW

View Article Online
View Journal | View Issue

Check for updates

Cite this: *Energy Environ. Sci.*, 2020, **13**, 1377

The role of carbon-based materials in enhancing the stability of perovskite solar cells

Mahboubeh Hadadian, *[a] Jan-Henrik Smått [a] and
Juan-Pablo Correa-Baena *[b]

Received 7th June 2019,
Accepted 6th March 2020

DOI: 10.1039/c9ee04030g

rsc.li/ees

Perovskite solar cells have been at the center of intense research over the past decade. Efficiencies have gone from single digits to a certified 25.2%, an unprecedented improvement for any solar cell technology. At this stage, stability remains a concern regarding the suitability of these solar cells for commercialization. Here, we review recent developments in the use of carbon materials to improve the stability of perovskite solar cells. Incorporating carbon materials into perovskite solar cells promises to be revolutionary in the solar cell field, as degradation mechanisms are alleviated to achieve long-term stability making them attractive for commercialization.

Broader context

Solar energy, as the cleanest and the largest exploitable resource of energy, can potentially meet the growing requirements for the whole world's energy needs beyond fossil fuels. An efficient route to convert solar energy into electricity is achieved by photovoltaics. Organic–inorganic metal halide perovskite solar cells have achieved power conversion efficiencies above 25% and are competitive to established technologies at half the price. The major obstacle of bringing perovskite solar cells to a pilot and consequently production line is the poor long-term device stability. Enhancing the stability of the layers as well as modifying the layer interfaces by replacing unstable components with more stable counterparts, or by incorporating stable additives, are vital measures for realizing long-term stable perovskite solar cells. In this context, carbon-based materials are the best candidates because of their stability, low-cost, and readily-available industrial-scale fabrication. This review aims to provide a comprehensive analysis of research progress in enhancing the stability of the perovskite solar cells by employing carbon-based materials. We conclude that carbon-based materials are crucial in providing stable perovskite solar cells while keeping costs low for scale-up and commercialization.

---

[a] *Laboratory of Molecular Science and Engineering, Åbo Akademi University, Porthansgatan 3-5, 20500 Turku, Finland. E-mail: mhadadia@abo.fi*
[b] *School of Materials Science and Engineering, Georgia Institute of Technology, Atlanta, GA, 30332, USA. E-mail: jpcorrea@gatech.edu*

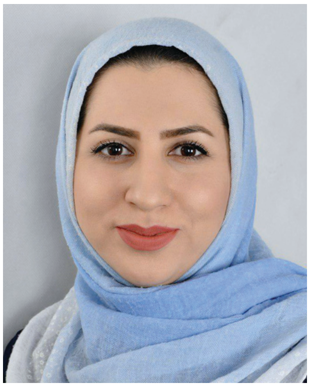

Mahboubeh Hadadian

Mahboubeh Hadadian is a postdoctoral researcher at Åbo Akademi University, Finland. She received her PhD in Physical Chemistry from Ferdowsi University of Mashhad, Iran, in 2016. During her PhD, she worked as a visiting student at École Polytechnique Fédérale de Lausanne (EPFL) University (Switzerland) in the group of Prof. Anders Hagfeldt focusing on the application of graphene derivatives in perovskite solar cells. She was awarded as the outstanding researcher at Ferdowsi University in 2016. Her recent research mainly focuses on designing and investigating stable perovskite solar cells.

Jan-Henrik Smått

Jan-Henrik Smått is a senior lecturer at Åbo Akademi University, Finland, from where he received his PhD degree in 2006. One year of his PhD work was carried out at the Max-Planck Institute for Coal Research in Germany. He also worked as a postdoctoral researcher in Prof. Christopher Landry's group at University of Vermont. He has been awarded two fellowships from the Academy of Finland and is currently the principal investigator of two national projects related to perovskite solar cells. His group focuses on the design of nanostructured materials for various renewable energy applications, including solar cells.

1. Introduction

Solid-state thin-film photovoltaic technologies offer the most promising pathways toward transforming solar energy into electricity in order to meet the growing global energy consumption needs.[1,2] Emerging thin-film solar cells such as organic solar cells, dye-sensitized solar cells, and most recently perovskite solar cells (PSCs) have emerged as low-cost solutions for solar cell deployment. While relatively simple deposition techniques and low capital expenditures promise a reduction in manufacturing cost, power conversion efficiencies (PCEs) need to be competitive with established technologies such as silicon solar cells. PSC technology is presently at the core of the interest in photovoltaic research owing to its impressive performance development in only a few years of research effort.[3]

The most widely used lead halide perovskite (LHP) has the potential to achieve an efficiency of 31%, according to theoretical calculations.[4] It could also reach higher PCEs if combined with other solar cell technologies to make tandem devices.[5] Since the pioneering work with an efficiency of 3.8%, PSCs have witnessed an ever-growing increase in efficiency. They have now achieved a lab-scale certified PCE of 25.2% rivaling the performance of commercial photovoltaic devices such as crystalline silicon or cadmium telluride (CdTe) solar cells.[6] Such a pronounced rise in PCE for new photovoltaic technology in such a short period of time is unprecedented in the history of photovoltaics. The exceptional performance is due to the advantageous optoelectronic properties, including large absorption coefficient, tunable bandgap, low exciton binding energy, ambipolar transport characteristics, high carrier mobilities, and long balanced carrier diffusion length of the LHPs.[7–9] The LHP takes on a structure of ABX_3, where A is an organic–inorganic cation such as methylammonium (MA), formamidinium (FA) or Cs, B is Pb or Sn, and X is a halide anion such as I, Cl and Br.[7]

Juan-Pablo Correa-Baena

Juan-Pablo Correa-Baena is an Assistant Professor at Georgia Tech. His group focuses on understanding and control of electronic dynamics at the nanoscale for semiconductors in solar cells and light emitting diodes. He received his PhD from UConn, USA, funded by two NSF fellowships. He worked as a postdoctoral fellow in the group of Prof. Anders Hagfeldt at EPFL. In 2017 he was awarded the US DOE postdoctoral fellowship to conduct work at MIT. He has published over 80 peer-reviewed papers (citations = 15 000; h-index = 44). In 2019 he was recognized by the Web of Science Group, Highly Cited Researchers-cross-field, and Nature Index, Leading early career researcher in materials science.

While the PCE of PSCs has increased dramatically, there are still some pending issues relating to scale up and commercialization. At this stage, the hunt is on to fabricate long-term stable PSCs.[2,10] The nature of LHP semiconductors and the ion migration effect entail the need for long-term stability data under real conditions.[11] The data on the outdoor stability of the PSCs is limited to only months, and the device lifetime is highly affected by the changes in real working conditions. In general, the combination of heat, light, and especially humidity results in the rapid degradation of PSCs.[12] In the presence of moisture, the formed hydrates could change the structure of the LHP crystals, which results in lower light harvesting.[13] Currently, the lifetime of the PSCs has extended from less than hours to 6 months and still, much work is needed before commercialization is viable.[10]

A variety of approaches have been applied in order to provide long-term stable PSCs. Improving the quality of the LHP film with less grain boundaries, using low-dimensional LHP, preventing the formation of ionic defects, applying protective layers around the LHP absorber, doping the LHP crystal by ions such as cesium are different approaches investigated for improving the stability of the devices.[10,14–16] Furthermore, altering different functional layers with more stable counterparts provides pathways for enhancing the stability of the PSCs. The use of carbon-based materials has been shown to be beneficial for the stability of the PSCs. Carbon materials tend not to react with halides and therefore they are tolerant to ion migration, inherently stable, and water-resistant (and can thus act as a hydrophobic moisture barrier).[15,17] Moreover, the relatively low-cost and readily-available industrial-scale fabrication of the carbon-based materials further promotes the commercialization of PSCs.[18] Carbon-based materials are versatile; for example, they exhibit different band energy alignments and their electronic properties can be tuned. Therefore, they have been used in almost all functional layers or as interface modifiers in PSCs. In this review, we summarize the developments in the application of the carbon-based materials for different functional layers of the PSC, highlighting their roles in enhancing the lifetime of PSC.

2. Carbon-based materials used in perovskite solar cells

Single junction PSCs have mainly two different configurations; n–i–p and p–i–n, where n, i, and p stand for donor-type, intrinsic, and acceptor type semiconductors, respectively. In mesoporous or planar regular (n–i–p) architecture, an electron selective layer (ESL) is deposited on a transparent conducting glass, which is followed by depositing the LHP layer. The hole selective layer (HSL) is deposited on top of the LHP film and topped by a metal contact. In the inverted (p–i–n) configuration, the bottom contact is selective for holes, while the ESL is on top.[2] Engineering the functional layers as well as the interfaces between the layers in PSCs has been widely studied to combat the stability challenge of PSCs.

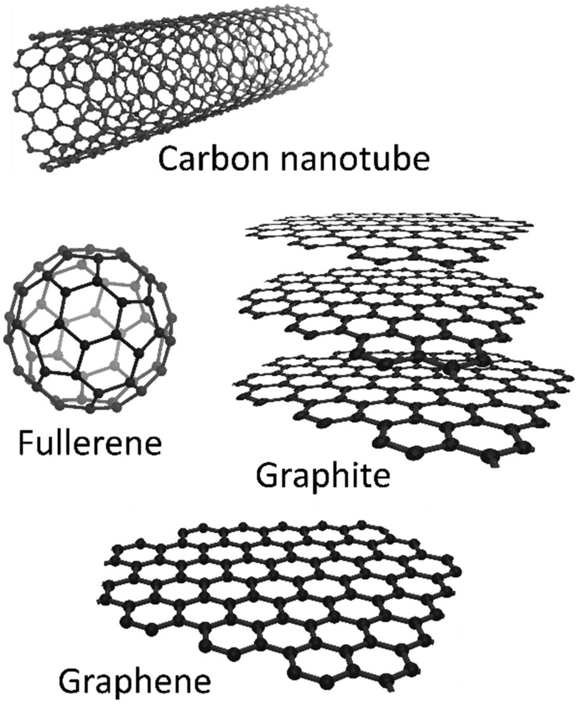

Fig. 1 Schematic structure of polymorphs of carbon.

Due to the various structures, carbon materials show different physical and chemical properties. Carbon-based materials applied in PSCs can be mainly divided into four categories, including fullerene and its derivatives, carbon nanotubes (CNTs), graphene (GR) and its derivatives, and other conductive carbon materials such as graphite and carbon black.[19] Fig. 1 shows the structures of the usual carbon materials, which will be reviewed herein.

If the carbon atoms bond randomly, paracrystalline carbon, namely "carbon black", is formed. Carbon materials possess features of accessibility, controllable porosity, chemical stability, low cost, and environmental friendliness, which are highly desired properties.[20] Owing to the multifunctional nature of carbon-based materials, they have been regarded as highly attractive materials in different layers of PSCs. Fig. 2 illustrates examples of applications of carbon-based materials in the functional layers or at the interface between the layers in PSCs. It will be explained in the following sections.

2.1 Fullerenes

Fullerene is a zero-dimensional (0D) cage-like arrangement of carbon atoms located at the nodes of a series of hexagons and pentagon.[21] It has been widely demonstrated that the use of fullerenes either as ESLs,[22] at the interface of the ESL and LHP layer,[23,24] or as additives in the LHP layer[25] can play an essential role in passivating the charge traps at the surfaces and grain boundaries, reducing the hysteresis, and electron extraction, which leads to higher device performances and stability.[26–29] Intrinsic single-crystalline LHPs have been reported to hold a considerable charge carrier diffusion length. However, in

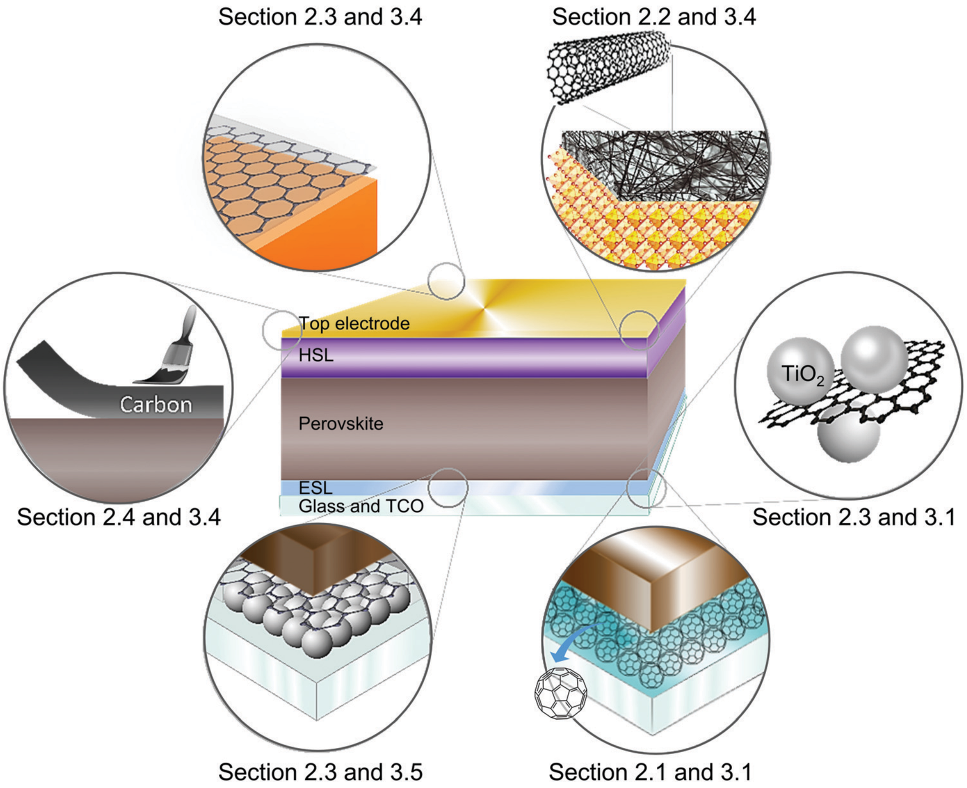

Fig. 2 Schematic illustration of the applications of carbon-based materials in different parts of the PSC. The device architecture (n–i–p) comprises a transparent conductive oxide (TCO) on top of a glass substrate, an electron selective layer (ESL), perovskite, a hole selective layer (HSL), and the top electrode.

real devices, numerous defects along grain boundaries in polycrystalline LHP films, induce non-radiative loss.[30–32] Passivating these trap-states *via* fullerene has been reported as an effective method to reduce the loss.

Due to their chemical nature, such as non-polarity and spherical shape, fullerenes behave as frames for the growth of LHP crystals.[32] This improves the morphology and increases the grain size of LHP.[32,33] Additionally, fullerenes can act as a barrier for moisture, thus enhancing long-term stability.[34]

Fullerene (C_{60}) was introduced into PSCs by Jeng and co-workers in 2013.[35] Fig. 3 shows the configuration (Fig. 3a) and energy levels of the devices (Fig. 3b). The matching of the lowest unoccupied molecular orbital (LUMO) level of fullerene with the conduction band edge level of LHP reduces the energy redundancy to achieve decent photovoltage output. However, these interlayers were not fairly explored due to the poor quality of the LHP film. Since then, rapid progress in p–i–n planar PSCs with various fullerene derivatives as ESLs has occurred, as summarized in Fig. 3c. Due to their electron affinity, efficient electron transport properties, low-temperature solution processable preparation, and suitable energy level alignment with LHPs, fullerene and its derivatives are the most used n-type ESLs in inverted PSCs.[36,37]

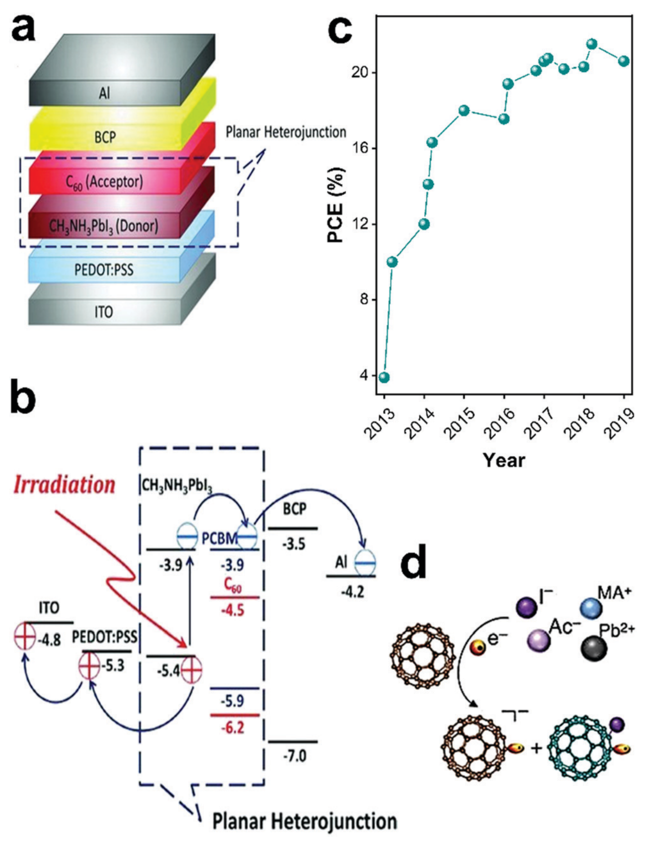

Fig. 3 Applying fullerenes in PSCs. (a) Schematic of the configuration of PSCs using PCBM as ESL. (b) Schematic of the energy levels of each layer in the device based on PCBM ESL, reproduced with permission.[35] (c) Summary of advances in device performance of p–i–n planar PSCs over the years applying fullerene-based ESLs (ref. 35, 38–51). The highest PCE value has been reported to be 21.5%.[48] (d) Details of the interaction of the LHP anions (I^-) and PCBM in hybrid solution, which results in PCBM radical anion and PCBM-halide radical, reproduced with permission under the Creative Commons license.[27]

Different fullerene derivatives such as *cis*-α-dimethoxy carbonyl fulleropyrrolidine C_{70} ($DMEC_{70}$), cross-linked silane-modified fullerene, and doped fullerene have been used as ESLs in p–i–n planar heterojunction structure[28,52,53] and later in the n–i–p architecture.[54] Umeyama *et al.*[55] reported for the first time the use of C_{60} thin films as the ESL in regular n–i–p PSCs, after thermal retro-Diels–Alder reaction on as-prepared glass/FTO/C_{60}-9-methylanthracene. Fullerene ESLs have also been doped with various materials such as decamethylcobaltocene,[56] oleamide,[29] carbon, and novel two-dimensional carbon materials such as graphdiyne[57] for application in PSCs.

The use of fullerenes as an additive within the LHP precursor solution,[58–60] in chlorobenzene as antisolvent[61] or by immersion of the as-prepared LHP thin films into a fullerene solution,[62] has shown remarkable FFs up to 86.7%, negligible hysteretic behavior, improved long-term-device stability, and high PCE values for large-area-based devices. One phenomenon believed to contribute to hysteresis behavior is the creation of charge trap states at the interfaces and crystal grain boundaries within devices.[63,64] Xu and co-workers[27] introduced LHP–PCBM hybrids to planar PSCs and explored the effect of PCBM in suppressing hysteresis. By its addition to the LHP solution, PCBM was claimed to be distributed throughout the LHP film between grain boundaries. PCBM passivated the iodide-rich trap sites on the surfaces of the grains and reduced anion migration through defects at grain boundaries, which was attributed to the formation of PCBM-halide radicals, Fig. 3d. Therefore, the incorporation of PCBM in the LHP active layer effectively suppressed the hysteresis behavior of the PSC.

PCEs of inverted PSC configurations have exceeded 20% using fullerene derivatives as the ESLs, as shown in Fig. 3c. Several fullerene derivatives with higher electron mobilities and hydrophobic properties have been designed for improving device performance as well as device stability. By tuning the physical and chemical properties of fullerenes, enhanced charge extraction and transport capabilities were obtained. In comparison to TiO_2, devices based on fullerenes as the ESLs have the advantages of low processing temperatures and suppressed *J–V* hysteresis. Moreover, the compatibility of the fullerene-based ESLs with the flexible substrates leads to further applications in light-weight flexible solar cells. We believe that by decreasing the structural disorder of fullerene derivative layers, it is possible to fabricate inverted PSCs with an improved V_{OC} comparable with that of TiO_2-based PSCs.

2.2 Carbon nanotubes

One-dimensional (1D) semiconducting materials such as CNTs, with unique structures, have been widely used in PSCs. CNTs are 1D hollow cylinders of carbon atoms which may be single-, double-, or multi-walled (SW-, DW-, and MWCNTs, respectively) and can vary in length, diameter, and chirality. Due to their unique structure and outstanding properties including excellent conductivity and high optical transparency, high chemical and thermal stability, exceptional electrical conductivities, and high surface area, CNTs have exhibited promising results when used in PSCs.[65–67] The unique extended π-system enables them to provide a direct pathway for charge transport with high mobility.[67] Extensive research has been focused on the application of CNTs in PSCs as they act mostly as charge collecting layer or additives to improve charge extraction, and enhancing the stability.

The electronic properties of various types of CNTs determine their function in solar cells. Metallic CNTs provide the continuous electronic pathway for charge transport. However, this type of CNTs lowers the performance of the device, if incorporated in the active layer.[68] For the photoactive layer, the desired type is semiconducting CNTs,[69] which could donate electrons to the external circuit or as an electron acceptor reducing the recombination of the charges.

Li *et al.*[70] performed one of the first studies on applying CNTs in PSCs using a laminated CNT network to replace the metal counter electrode in n–i–p architecture (Fig. 4a and b). CNTs functioned as both HSL and electrode showing 6.9% efficiency with dual side illumination possibility due to the transparency of the CNT film. The low efficiency was probably due to the relatively high resistance of the CNT film and a lack of charge-selectivity. Therefore, incorporating spiro-OMeTAD improved the performance yielding a PCE of 9.9%.

Aitola *et al.*[66] fabricated a PSC by depositing a double-SWCNT film on the LHP layer and then drop-casting spiro-OMeTAD. The solar cell showed 15.5% efficiency without the application of a metal top electrode. A cross-sectional scanning electron microscopy (SEM) image of the device structure is shown in Fig. 4c. The long "whiskers" in the solar cell cross-sectional SEM image are supposed to be SWCNTs separated from the film during cleavage of the device. A review on the incorporation of CNTs as charge conduction layer in PSCs is given by Habisreutinger *et al.*[73]

Benefiting from the unique properties of CNTs, namely their excellent charge transport characteristics together with inherent mechanical flexibility[71,74] the impressive application of CNTs, especially for portable devices, is their use in flexible fiber-shaped PSCs.[75] Qiu *et al.*[71] fabricated PSCs with a flexible fiber structure in which the LHP absorber is sandwiched between an n-type core wire and the flexible p-type nanotubes (Fig. 4d). The cathode forming the outermost layer is a sheet of aligned CNTs that were dry-drawn from a spinnable array. The fiber-shaped PSC exhibited a PCE of 3.3%, which remained stable on bending. The efficiency of these devices has thus far not exceeded 10%, but for a photovoltaic fabric, this is very promising.

SWCNT and MWCNT have been found to perform very well when incorporated in or used solely as the HSL in PSCs.[76,77] CNTs efficiently replace p-type dopants in common HSLs (spiro-OMeTAD and P3HT), particularly when their poor dispersibility for solution-processability is modified through functionalization. Habisreutinger *et al.*[72] showed that CNTs could replace the doping required for spiro-OMeTAD by employing a two-layered structure of polymer-wrapped CNTs embedded within an organic matrix. The device had more efficient charge extraction in comparison to the device with undoped spiro-OMeTAD. However, its efficiency was lower than the state-of-the-art PSC probably because the nanotubes in this configuration cannot effectively form a closely interconnected percolation network, resulting in the device being limited by series resistance (R_s) and thus limiting the fill factor. Being randomly dispersed through the spiro-OMeTAD layer, the CNTs did not have enough direct interfacial contact with the LHP absorber to transport holes from the interface efficiently. When CNTs and spiro-OMeTAD were deposited sequentially (as shown in Fig. 4e), CNTs formed a densely interconnected network with a direct interface with the LHP layer. It provided efficient transfer of photogenerated holes from the absorber facilitating selective hole transport.

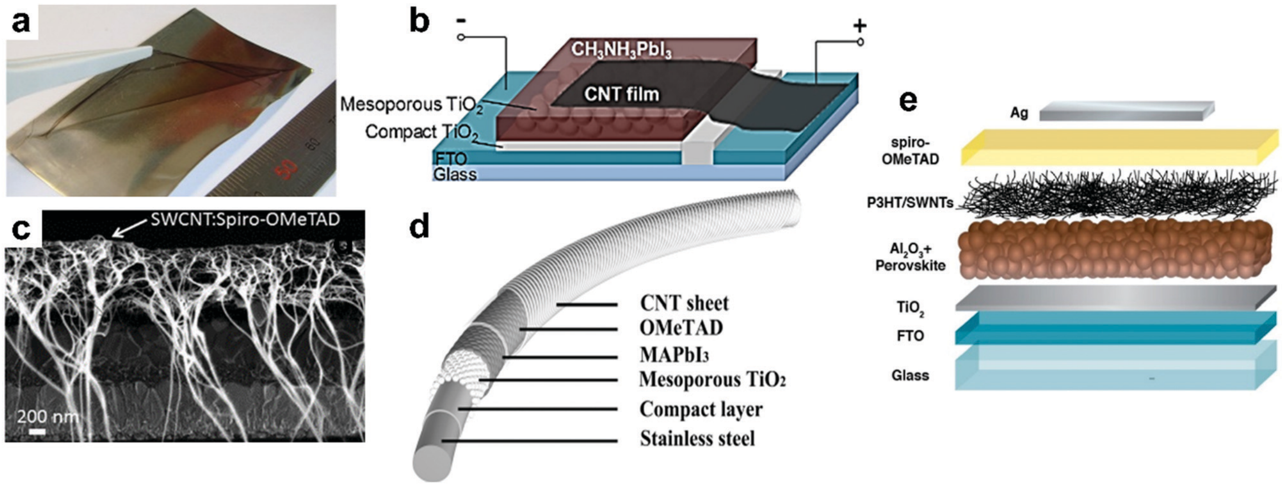

Fig. 4 CNTs in PSCs. (a) Photo of freestanding CNT film lifting by tweezers to transfer onto other substrates. (b) Schematic of $CH_3NH_3PbI_3$ PSC with CNT film electrode, reprinted with permission.[70] (c) Cross-sectional SEM image of cells with SWCNT:spiro-OMeTAD, reprinted with permission.[66] (d) Structure of the fiber-shaped PSC, reprinted with permission.[71] (e) The schematic architecture of a device with a P3HT/SWNT layer underneath the hole transport material (spiro-OMeTAD) matrix, reprinted with permission.[72]

The inherent resilience and stability of CNTs are the most important advantages when applied in solar cells. Several approaches have been reported for utilizing the charge transport properties of CNTs to extract photogenerated charges in PSCs. The use of entirely solution-processed CNT structures for replacing the costly components of PSCs, such as metal counter electrodes and commonly used HSLs, can be determining for the future of this technology.[78] It makes the PSCs more cost-effective and at the same time more environmentally-friendly. Further improvements in the PCE of devices based on CNT components could make them a highly competitive and advantageous option for high-performing stable devices.

2.3 Graphene and its derivatives

GR is a two-dimensional (2D) sheet with sp^2 hybridized carbon atoms arranged in a honeycomb lattice. It exhibits superior electronic, mechanical, and optical properties, ambipolar electrical characteristics, and high flexibility suitable for optoelectronic applications.[79] GR sheets can be stacked to form three-dimensional (3D) graphite, rolled to form 1D CNTs, and wrapped to form 0D fullerenes.[80,81] GR and its derivatives have been widely used in energy efficient applications for realizing high performance, low cost, light weight, and flexible energy devices to meet the limited energy resources worldwide. Particularly, GR and GR oxide (GO) have found roles in PSCs as ESLs and HSLs (due to the ambipolar nature), electrodes, inside the LHP layer, and at the interfaces between layers.

GR has been used as an electrode in semitransparent PSCs.[82] The GR layer was prepared *via* chemical vapor deposition (CVD) on a copper foil, which was then coated with a poly(methyl methacrylate) (PMMA) layer and a thin layer of poly(dimethylsiloxane) (PDMS) (as a supporting layer). To optimize the functioning of GR as an electrode, a thin layer of PEDOT:PSS was deposited on the GR surface as an adhesive layer to the LHP film. It not only reduced the sheet resistance of the GR but also induced p-type doping of the GR electrode. Fig. 5a shows a schematic of the device configuration of this semitransparent PSCs. The prepared device with a double-layer of GR showed 12.02% efficiency from the fluorine-doped tin oxide substrate side (FTO) and 11.65% from the GR side. GR has also been used as the electrode in flexible PSCs with high bending durability because of its excellent mechanical flexibility.[83] However, the hydrophobic nature of GR poses challenges for application as the electrode in PSCs due to wettability issues.[84]

Although the direct fabrication of GR by CVD results in high-quality layers, the reduction of GO is a more cost-effective approach. Yan and co-workers[88] applied single-layered GR (SG) and multi-layered GR (MG) derived from the reduction of GO as a hole extraction electrode in PSCs. SG and MG had different work functions (4.8 eV for SG and 5.0 eV for MG). For hole extraction, MG worked better than SG due to the as-formed Schottky barrier. The energetic difference results in ohmic contact and a Schottky junction with the LHP (Fermi level at −4.73 eV). MG/LHP interface was assembled as a Schottky junction, with a rectifying characteristic, which afforded hole extraction and electron rejection effectively, whereas the SG/LHP interface showed an ohmic contact behavior, whose charge selective capability is not as good as for MG. To date, however, the nature of the interface between LHP and nanocarbon hole extraction electrodes has not been addressed well.

The high-temperature required for the sintering of ESLs based on TiO_2 increases the production costs of the PSCs and limits their applicability on flexible plastic substrates and in multi-junction device architectures.[89] Applying a GR–TiO_2 nanocomposite processed at low temperature (150 °C) behaved as an efficient ESL and avoids the high-temperatures needed for the sintering of ESLs.[90] The best performing device based on a GR–TiO_2 nanocomposite yielded a PCE of 15.6%. The fabrication of TiO_2 ESL at low temperatures develops a low-temperature processing route for mesoscopic PSCs. To date, in comparison to the functional layers in PSCs, minimal improvement in efficiency and durability has been shown when incorporating GR-based materials at the LHP/ESL interface. A layer of lithium-neutralized GO (GO-Li) between TiO_2 and the LHP layer improved the electron extraction from the active layer into the mesoporous TiO_2.[91] Integrating GO-Li as an interlayer between TiO_2 and the LHP layer resulted in the enhancement of J_{SC}, FF, and therefore in the PCE. The main reason for this enhancement is because the substitution of H atoms in the carboxyl groups of GO by Li atoms decreased the work function of GO (from 4.9 to 4.3 ± 0.1 eV). It provided an energetically aligning of GO with the conduction band of TiO_2.

The incorporation of different GR derivatives in the LHP layer can enhance the photovoltaic performance of the PSCs.[85,86,92] GR quantum dots (GQDs) were incorporated into the LHP layer to minimize the charge recombination at the LHP grain boundaries by passivating trap states and enhancing electron extraction (Fig. 5b).[85] By adding 7% GQDs into the active layer, the solar cells showed 17.62% PCE (the PCE of reference device without GQDs was 16.29%).

Nitrogen-doped reduced GO (N-RGO) was integrated into the LHP layer which resulted in bigger grain sizes of the LHP (Fig. 5c (left)).[86] The increase in grain size was due to the interaction between formamidinium cations in the LHP precursor solution and nitrogen groups on the GR structure which slowed down the crystallization of the LHP, Fig. 5c (right). In addition, the introduction of this GR derivative in the LHP precursor solution also resulted in surface passivation of the LHP grains.

GO can be made *via* cost-effective solution-based processing and in comparison to GR, GO-based materials are more suitable as HSLs in PSCs, due to the better band alignment with the valence band of the $MAPbI_3$ LHP (5.4 to 6 eV).[93,94] The work function of GO is about 4.9 eV[95] which is higher than that of pristine GR (*i.e.*, 4.5 eV). A high work function would create an ohmic contact, which increases the built-in potential for higher V_{OC}, while a high conductivity would lead to a high FF due to improved charge collection. It has been used as an alternative for poly(3,4-ethylenedioxythiophene):poly(styrene sulfonate) (PEDOT:PSS) (which has inefficient electron blocking potential and poor stability in the LHP precursor solvent) in p–i–n heterojunction with good surface coverage and enhancing the crystallization of the LHP layer.[96,97]

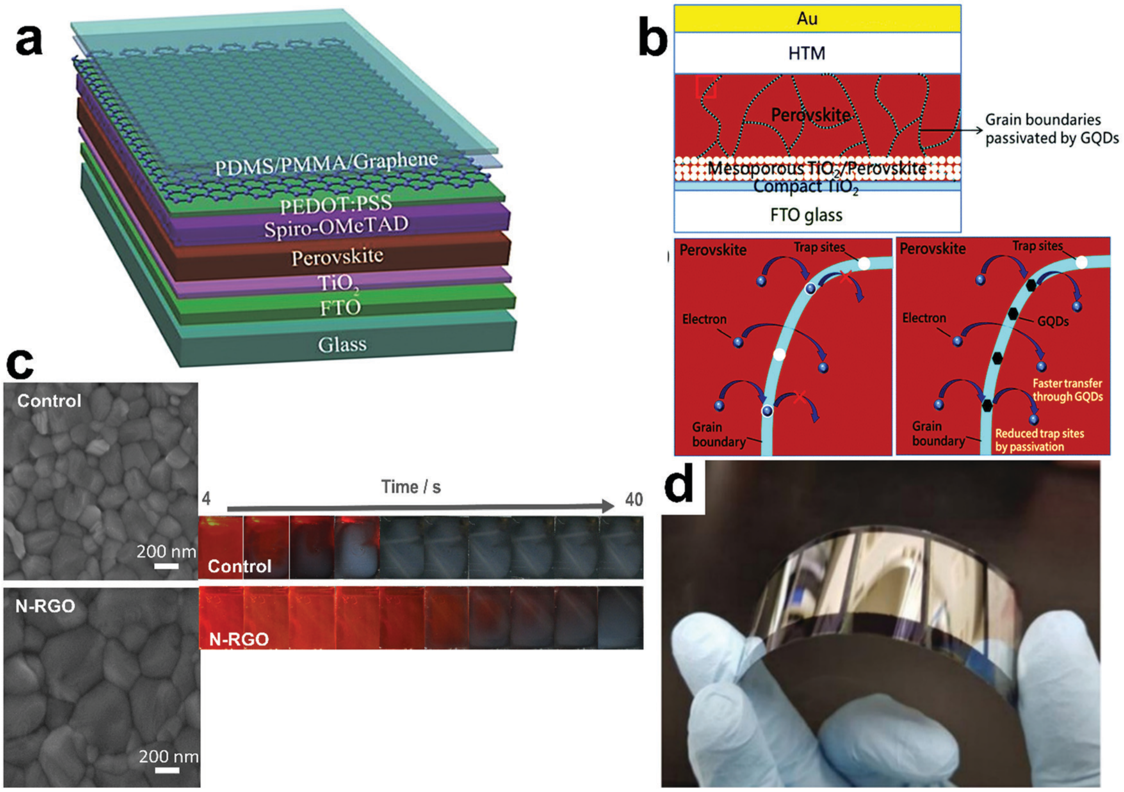

Fig. 5 Graphene-based materials in PSCs. (a) Schematic of the configuration of a semitransparent PSC with GR-based electrodes, reprinted with permission.[82] (b) Schematic of the device structure of PSC and reducing the recombination of charge carrier by GQDs, reproduced with permission.[85] (c) Left: SEM top-view images of pristine perovskite (control) and perovskite/N-RGO hybrid films (N-RGO). Right: Photographs of LHP films during crystallization at 100 °C, which shows the slower formation of the LHP layer in the presence of N-RGO in comparison to pristine perovskite, reproduced with permission.[86] (d) Photograph of the flexible PSC mini-module where a fluorinated RGO is added to the HSL based on a PEN substrate, reprinted with permission.[87]

It is still challenging to achieve both a high work function and conductivity in GO.[98] It contains a large number of oxygen functional groups resulting in a high work function. However, this large amount of oxygen content causes very low conductivity in the material, which is a limiting factor for efficient hole transport. Therefore, in order to obtain high performance for both the work function and the conductivity has to be carefully balanced.[98]

RGO, which has a lower band gap energy than GO, has been used as a promising candidate to overcome this disadvantage.[87,99] An improvement in the performance of planar PSCs was achieved by Yeo *et al.*[87] using a solution-processed fluorinated RGO as HSL, which resulted in 10.0% PCE. The molecularly-doped RGO showed a fast charge-extraction ability and also promoted LHP crystallization. It is worth noting that PSC modules were prepared on a flexible polyethylene naphthalate (PEN)/ITO substrate (Fig. 5d), which showed a PCE of 8.1%.

Graphdiyne is a new 2D carbon allotrope with a structure like GR, with sp- and sp^2-hybridized carbon network which possesses highly conjugated structure.[100] It has a rigid carbon network, remarkable electronic properties, and a natural band gap.[101] Graphdiyne was used as an additive in P3HT. The strong π–π interaction between Graphdiyne and P3HT resulted in superior photovoltaic performance. The devices showed 15.58% PCE compared to 11.53% for devices with pristine P3HT. Furthermore, preliminary stability tests indicated that unsealed devices stored in a desiccator retained 90% of its initial PCE after 15 weeks, which is the same as for the one with P3HT HSL.[102]

The particular features of GR and its derivative, including unique electronic, optical, chemical, and mechanical properties, have been largely exploited in the field of photovoltaic conversion. One notable advantage of GR is its scalable solution-processable fabrication. The first demonstration of GR used in the context of hybrid PSCs was reported at the end of 2014. Nevertheless, significant advances have been already achieved, which demonstrates the tremendous potential of this material in PSCs and tandem devices. Table 1 shows the solar cell parameters of GR-based PSCs.

2.4 Graphite and carbon black

3D graphite is an abundant historical carbon material with relatively high electrical conductivity, high surface area, and thermal stability.[130–132] Together with carbon black to form better contact, graphite is mainly chosen as the counter electrode in solar cells.[133] The work function of carbon (~5.0 eV) ensures an efficient hole extraction from the LHP to the carbon layer. Furthermore, carbon black shows certain conductivity, as well as high surface-area-to-volume ratio. In 2013, carbon materials

Table 1 Summary of the representative functions of GR and its derivatives in PSCs

Material	Function$^{\mathrm{ref.}}$	Effect	Device structure	J_{SC} (mA cm^{-2})	V_{OC} (V)	FF (%)	PCE (%)
GR	Top contact Anode[82]	Both-side illumination	FTO/c-TiO$_2$/MAPbI$_{3-x}$Cl$_x$/spiro-OMeTAD/PEDOT:PSS/GR(PDMS/PMMA/GR film)	17.7	0.94	72	12.0
	Anode[84]	PCE↓	GR/MoO$_3$/PEDOT:PSS/MAPbI$_3$/C$_{60}$/BCP[a]/LiF/Al	21.1	1.03	72	16.1
	Anode[103]	—	GR/c-TiO$_2$/mp-TiO$_2$/MAPbI$_{3-x}$Cl$_x$/spiro-OMeTAD/Au	2.55	0.69	35	0.62
	Anode[104]	PCE↓ Mechanical stability↑	PEN/GR/MoO$_3$/PEDOT:PSS/MAPbI$_3$/C$_{60}$/BCP/LiF/Al	21.7	1	78	16.8
	Interfacial layer[105]	Stability↑	FTO/c-TiO$_2$/GR flakes + mp-TiO$_2$/GO-Li/MAPbI$_3$/spiro-OMeTAD/Au (large-area)		8.57	65	12.6
	ESL[106]	Stability↑	ITO/PEDOT:PSS/MAPbI$_3$/PCBM/GNPs[b]/Al	18.5	0.98	78	14.3
	In ESL[107]	PCE↑	FTO/c-TiO$_2$/mp-GR/SrTiO$_3$/MAPbI$_3$/spiro-MeOTAD/Ag	20	1.03	72	14.5
	In ESL[108]	PCE↑ Stability↑	ITO/SnO$_2$:NDI[c]–GR/FA$_{0.75}$MA$_{0.15}$Cs$_{0.1}$PbI$_{2.65}$Br$_{0.35}$/spiro-OMeTAD/Au	22.7	1.08	82	20.2
	Electrode and in ESL[109]	PCE↑ Mechanical stability↑	GR/PCBM:GQDs/MAPbI$_3$/PTAA/Au	20.8	1.07	74	16.4
	EDS layer[110]	PCE↑ UV stability↑	N-GQD EDS[d]/FTO/TiO$_2$/γ-CsPbI$_3$/PTAA/Au	19.2	1.11	76	16.2
	ESL[111]	PCE↑	FTO/GQD@SnO$_2$/Cs$_{0.05}$((FAPbI$_3$)$_{0.83}$(MAPbBr$_3$)$_{0.17}$)$_{0.95}$/spiro-OMeTAD/Au	23.5	1.08	77	19.6
		Mechanical stability↑	PEN/ITO/GQD@SnO$_2$/spiro-OMeTAD/Au	22.1	1.07	75	17.7
	ESL[112]	PCE↑ Light and thermal stability↑	FTO/ZnO/GR/LHP/spiro-OMeTAD/Au	22.7	1.12	78	19.8
	ESL[113]	PCE↑ Stability↑	FTO/c-TiO$_2$:GNRs[e]/mp-TiO$_2$:GNRs/MAPbI$_3$/spiro-OMeTAD/Ag	23	1.05	73	17.7
RGO	Interfacial layer[114]	Light and thermal stability↑ PCE↓	FTO/c-TiO$_2$/mp-TiO$_2$/FAMACsPbI$_{3-x}$Br$_x$/CuSCN/RGO/Au	23.2	1.11	78	20.4
	In ESL[115]	PCE↑	FTO/c-TiO$_2$/RGO–mp-TiO$_2$ nanocomposite/MAPbI$_3$/spiro-OMeTAD/Ag	22	0.93	71	14.5
	In ESL[116]	PCE↑ Stability↑	FTO/ZnO–RGO/MAPbI$_3$/spiro-OMeTAD/Au	21.7	1.03	68	15.2
	In ESL[117]	PCE↑	FTO/c-TiO$_2$/mp-TiO$_2$:RGO(Li treated)/(FAPbI$_3$)$_{0.85}$(MAPbBr$_3$)$_{0.15}$/spiro-OMeTAD/Au	22	1.11	80	19.5
	In ESL, LHP, and HSL[118]	PCE↑ Stability↑	FTO/RGO–TiO$_2$/RGO–MAPbI$_3$/RGO–spiro-MeOTAD/Ag	22.9	1.00	72	16.5
	ESL[119]	PCE↑	FTO/c-TiO$_2$:RGO/mp-TiO$_2$:RGO/MAPbI$_3$/spiro-MeOTAD/Au	16.5	0.84	68	9.3
	In LHP[86]	PCE↑	FTO/c-TiO$_2$/mp-TiO$_2$/(FAPbI$_3$)$_{0.85}$(MAPbBr$_3$)$_{0.15}$:N-RGO/spiro-OMeTAD/Au	21.8	1.15	74	18.7
	In LHP[120]	PCE↑ Stability↑	FTO)/SnO$_x$/(Cs$_{0.05}$(FA$_{0.85}$MA$_{0.15}$)$_{0.95}$Pb(I$_{0.85}$Br$_{0.15}$)$_3$:oxo-RGO/DA[f])/spiro-OMeTAD/Au	23.1	1.13	81	21.1
	HSL and anode[88]	PCE↑	FTO/c-TiO$_2$/mp-TiO$_2$/MAPbI$_3$/RGO	16.7	0.94	73	11.5
	HSL[99]	PCE↑ Stability↑ Reproducibility↑	ITO/RGO/MAPbI$_3$/PC$_{61}$BM/BCP/Ag	14.8	0.95	71	10.8
	Interfacial layer[121]	PCE↑	ITO/c-TiO$_2$/MAPbI$_3$Cl$_{3-x}$/RGO/spiro-OMeTAD/Au	21.5	1.11	78	18.8
	In HSL[122]	PCE↓ Stability↑	FTO/TiO$_2$/MAPbI$_3$/spiro-OMeTAD + RGO/Au	16.7	0.91	0.6	10.6
	HSL[123]	PCE↑ Stability↑	ITO/RGO/MAPbI$_3$/PCBM/Ag	21.3	0.96	79	16
	Transparent electrode[103]	PCE↓	RGO/c-TiO$_2$ + GR/mp-TiO$_2$ + GR/MAPbI$_{3-x}$Cl$_x$/spiro-OMeTAD/Au	2.9	0.69	38	0.81
GO	In HSL[95]	PCE↑	ITO/PEDOT:PSS:AgOTf-doped[g] GO/MAPbI$_{3-x}$Cl$_x$/PCBM/Au	19.2	0.88	71	11.9
	HSL[124]	PCE↑ Stability↑	ITO/ammonia-treated GO/MAPbI$_{3-x}$Cl$_x$/PC$_{61}$BM/BCP/Ag	18.4	1.00	77	14.14
	Interlayer[91]	PCE↑ Stability ↑ Hysteresis↓	FTO/c-TiO$_2$/mp-TiO$_2$/GO-Li/MAPbI$_3$/spiro-OMeTAD/Au	19.6	0.86	70	11.8
	In LHP[125]	PCE↑	FTO/spiro-bifluorene/GO–MAPbI$_3$/PC$_{61}$BM/Au	18.8	1.07	71	14.3
	HSL[96]	PCE↑	ITO/GO/MAPbI$_{3-x}$Cl$_x$/PCBM/ZnO/Al	17.5	1	71	12.4

Table 1 *(continued)*

Material	Function$^{ref.}$	Effect	Device structure	J_{SC} (mA cm^{-2})	V_{OC} (V)	FF (%)	PCE (%)
	HSL[126]	PCE↓	ITO/GO/$MAPbI_{3-x}Cl_x$/PCBM/BCP/LiF/Al	14.5	0.92	72	9.6
	In LHP[127]	PCE↑ Stability↑	ITO/GO/$MAPbI_3$:GO/PCBM/Ag	20.7	0.93	65	15.2
	Interfacial layer[128]	PCE↑	ITO/PEDOT:PSS-GO:NH_3/$MAPbI_{3-x}Cl_x$/$PC_{61}BM$/Bphen/Ag	21.7	1.03	70	16.1
	Interfacial layer[129]	PCE↑	FTO/c-TiO_2/mp-TiO_2/$MAPbI_{3-x}Cl_x$/GO/P3HT/Au	24.4	0.93	58	13.2

[a] Bathocuproine. [b] Graphene nano platelets. [c] *N*,*N*′-Bis-[2-(ethanoic acid sodium)]-1,4,5,8-naphthalene diimide surfactant. [d] Energy-down-shift layer. [e] Graphene nanoribbons. [f] Oxo-functionalized graphene/dodecylamine. [g] Silver trifluoromethanesulfonate.

were first applied in PSCs in the form of a fully-printable carbon counter electrode by Ku *et al.*[134] In this study, a carbon black/spheroidal graphite mixture was used as the main component of the carbon paste in the counter electrode.

The electrical conductivity of carbon electrodes strongly depends on the thermal treatment. Consequently, this type of carbon paste needs to be sintered at a high temperature of 400–500 °C to form a well-conducting carbon counter electrode. Because the LHPs will decompose at temperatures beyond 200–250 °C,[135] the device fabrication technology was further developed to become namely a HSL-free PSC with carbon electrode (C-PSC). The device was fabricated by preparing a mesoscopic C-PSC with a multi-layer mesoporous architecture consisting of TiO_2, ZrO_2, and carbon layers, which were screen-printed on a FTO/compact TiO_2 substrate. The LHP precursor solution was drop-casted onto the carbon black/graphite layer resulting in 6.6% PCE.[134] In general, the fabrication process is to sequentially deposit a TiO_2 scaffold layer, a ZrO_2 or Al_2O_3 insulating spacer layer, and a mesoporous carbon layer. Then, the LHP precursor solution is infiltrated through the three layers (carbon, spacer, and $TiO_{2)}$. Because LHP crystals form in a mesoporous TiO_2/ZrO_2/carbon scaffold for PSCs,[17] the structure of the mesoporous films directly affects the particle size and uniformity of LHP crystal. It has a great influence on the photovoltaic performance of the solar cell.

Moderate progress on the performance of C-PSCs has improved the PCE, which is still 16%.[136–138] Fig. 6a shows a summary of the development in PCEs of C-PSCs in comparison to state-of-the-art PSCs since 2013. Based on the structure and

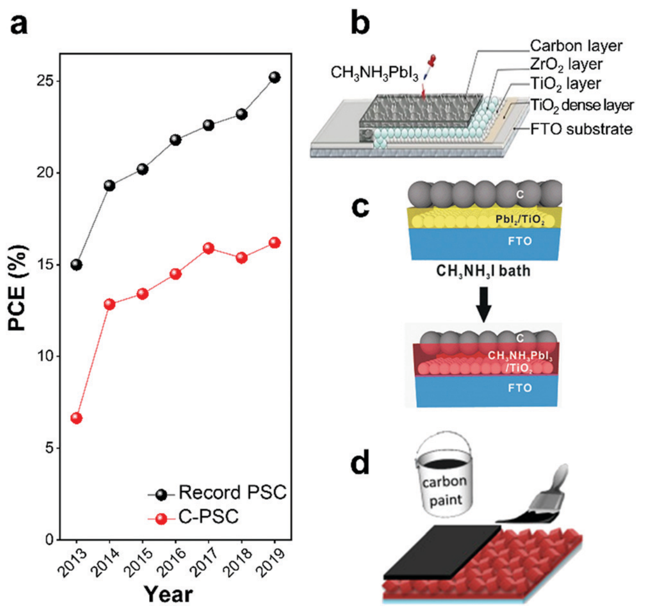

Fig. 6 Summary of development and structures of C-PSCs. (a) Summary of development in PCEs of C-PSCs ref. 54, 134, 139–143 in comparison to state-of-the-art PSCs.[6] The PCE of the C-PSCs has reached 16.2%,[143] while the highest PCE of state-of-the-art PSC is 25.2%.[6] Structure and fabrication processes of three types of C-PSCs: (b) meso C-PSC, reprinted with permission,[134] (c) embedment C-PSC, reprinted with permission,[144] and (d) paintable C-PSC,[145] reprinted with permission.[146]

fabrication procedure, C-PSCs can be classified into three different types; meso, embedment, and paintable C-PSCs (shown schematically in Fig. 6b–d).

Meso C-PSC architecture consists of a multi-layer mesoporous structure, typically, a double layer of mesoporous TiO_2 and ZrO_2 covered by a porous carbon layer (TiO_2/ZrO_2 or Al_2O_3/porous carbon film),[17] as shown in Fig. 6b. The carbon layer is deposited *via* doctor-blading or screen printing of carbon paste containing graphite, carbon black, and ZrO_2 (or Al_2O_3) nanoparticles. An LHP precursor solution subsequently infiltrates the porous structure.[134,139,147] Meso C-PSCs can also be made through a two-step process. In this method, PbI_2 is deposited on the mesoporous structure followed by chemical conversion to LHP.[137]

Embedment C-PSC was developed as a simplified fabrication method to prevent the high-temperature process.[148] The carbon electrode is deposited onto the PbI_2 layer by spin coating of carbon-based materials such as carbon black, CNTs, graphite, and GR. This is followed by converting PbI_2 to LHP ($MAPbI_3$), Fig. 6c. Wei *et al.* deposited carbon electrodes using inkjet printing of carbon on top of the PbI_2 layer, followed by conversion to the LHP. In another strategy, carbon/MAI ink was printed on top of PbI_2, resulting in a simultaneous chemical conversions of PbI_2 to LHP. The use of carbon/MAI and *in situ* transformation of PbI_2 to LHP constructed a seamless interface between the LHP layer and the carbon electrode. Therefore, charge recombination decreased compared to when carbon ink was used.[144,147]

Fig. 6d shows paintable C-PSCs in which the carbon electrode is fabricated by depositing a paste or paint of carbon on a pre-deposited LHP layer either by painting or doctor blading. A typical architecture of this type of C-PSCs is FTO/TiO_2/LHP/carbon.[17,147]

Due to improved long-term stability, low production costs, and high upscaling potential, C-PSCs have become an important field of study within the PSC community.[139,149–153] Recent developments on device structure and working principles of the three types of C-PSCs have been reviewed by Chen and Yang.[147]

PSCs with conventional structure usually employ organic HSLs (spiro-OMeTAD or PTAA) to collect holes efficiently. However, these HSLs hinder the stability of PSCs. Removing HSL can improve stability, reduce the cost, and simplify the fabrication process. On the other hand, the noble metal (Ag or Au) fabricated by thermal evaporation under a high vacuum condition still represents high cost and high-energy consumption. Conductive carbon materials, possessing the benefits of low-cost, earth-abundance and printable, are a promising candidate to achieve high-performing and low-cost hole-conductor-free C-PSCs.[17]

3. Stability of perovskite solar cells containing carbon-based materials

Degradation of PSC is affected by various parameters whose impact is still not fully understood. The degradation takes place due to environmental factors or due to the intrinsic instability of the LHP or any intermediate layers.[154,155] The external parameters include humidity, oxygen, heat, light, and applied electrical bias.[155,156]

Of the external causes affecting PSC stability, moisture and oxygen are two of the most pervasive.[10,155] The instability of PSCs in humid conditions originates from the hygroscopic nature of the amine salt. In $MAPbI_3$, the methylamine group is lost *via* sublimation leading to the formation of PbI_2. The LHP absorbs water from the surrounding environment leading to hydrated LHP phases that alter the structures of crystal. This change lowers the ability of the LHP to absorb the visible light.[10,157]

Under working conditions, direct exposure to sunlight increases the temperature of solar cells and high temperature is one cause for PSCs degradation. The thermal degradation occurs even under inert conditions.

This degradation occurs because of the thermal instability of the LHP or unstable layers such as the HSL. It is well-known that temperature has a significant impact on the phase and crystal structure of the LHP.[157] Light is another reason for degradation in PSC. Initially, this decomposition mechanism was thought to be caused by moisture. Nevertheless, it has been observed that severe decomposition occurs during the illumination even in the dry air. When the LHP is exposed to illumination in dry air, it decomposes into its components. For instance, $MAPbI_3$ decomposes into methylamine, PbI_2, and I_2 as reaction products. The photo-induced electrons in the LHP react with oxygen molecules forming superoxide, which further reacts with methylamine.[157,158]

Another degradation effect is the decomposition of the LHP due to electrical bias. The electric field triggers both functional and structural transformations in PSC.[159] The influence of external electric bias is to cause ion migration in the solar cell (due to the low activation energy) or charge carrier accumulation that results in thermally activated trap formation or unfavorable electrochemical reactions.[155,160] Therefore, applied electric fields, both positive and negative biases, are potentially harmful and can cause PSC degradation.[13,160]

The instability of the device comes mostly from the degradation of the inherently poor stability of the LHP materials. Relatively weak Pb–I bonds combined with high ion migration make the LHP susceptible to degradation *via* a wide variety of degradation mechanism. The problem is intensified when the LHP is combined with other components in the PSC, such as the ESL, HSL, and metal contact.

Several studies have discussed the influence of different conditions such as humidity, temperature, and light on the degradation of the PSCs and have investigated different methods for enhancing the stability of the PSCs. Among the various methods for improving the stability of PSCs, the application of carbon-based materials seems to be one of the most promising approaches for addressing the challenge of outdoor stability. Carbon-based materials are thermally stable, they have been shown not to interact with the halides in LHPs, and they are inherently water-resistant.[2,134,147] The long-term stability of PSCs has been evaluated in different ways including dark storage of the devices on a shelf called cold or hot drawer test, maximum power point (MMP) tracking, and outdoor tests.[2,11] In the following sections, we discuss the improvement in the stability of the PSCs by using the carbon family materials in different functional layers of the devices.

3.1 Electron selective layer

The performance and stability of PSCs are strongly dependent on the choice of ESL.[7,94] Both metal oxides and polymers have been used as n-type semiconductor ESLs in PSCs. ESL plays a vital role in the performance of PSCs by facilitating the extraction of photogenerated electrons from the LHP layer and transferring them to the conducting electrode. In the mesoscopic n–i–p PSCs, TiO_2 compact layers is typically used which is topped by a mesoporous semiconductor scaffold such as TiO_2, SnO_2, and WO_3.[89] Due to the ambipolar transport behavior of the LHP and long diffusion lengths, the mesoporous scaffold layers can also be composed of metal oxide insulators like Al_2O_3, ZrO_2, and SiO_2, and it has been shown that PSCs are highly efficient even without a scaffold.[94,161]

Owing to the high selectivity and proper conduction band (which is well-matched with the LHP layer), TiO_2 and SnO_2 are currently the most common ESLs in state-of-the-art PSCs.[23] However, the photocatalytic activity of TiO_2, which is utilized in different applications such as pollution abatement in water or air,[162] has become an issue in PSCs hindering the stability of the devices.[54] The reduced device stability can also be attributed to adsorbed water and oxygen at the TiO_2 surface.[163] As an alternative, n-type materials like electron-transporting carbon materials have been applied to increase the stability of the PSCs either by replacing the ESLs or by incorporating carbon materials into the conventional ESLs.

SWCNT-incorporated TiO_2 nanofibers[161] as well as TiO_2 nanoparticles[164] have been demonstrated as ESLs by Batmunkh *et al.* The introduction of SWCNTs in the ESL induced suitable energy levels and decreased charge recombination.

Combining two 1D materials as ESL led to devices with fast charge extraction and low recombination rates. PSCs with SWCNT incorporated in the TiO_2 nanofibers photoelectrodes showed 40% enhancement in efficiency as compared to the control devices with only TiO_2 nanofibers. The conductive SWCNTs incorporated in TiO_2 nanofibers provided a fast electron transfer within the photoelectrode, increasing the J_{SC} value. Alongside an increase in PCE, these devices also showed improved stability both in light and under humid conditions. Fig. 7a shows the stability tracking of the unencapsulated devices based on TiO_2 nanofiber ESLs with and without SWCNTs for 288 h under ambient storage conditions at a relative humidity of 60%. The performance of the control device dropped to 10% of the original efficiency after 288 h, while the devices with TiO_2 nanofibers and SWCNTs dropped to 34%. The humidity causes changes in the morphology and decomposition of the LHP layer.[161] These morphological changes affect the electron transfer from LHP to TiO_2. Presence of CNTs or GR derivatives[116] in ESL could provide better connectivity between ESL and LHP. Therefore, extra charge carrier pathways mitigate the changes in LHP layer.[116,161]

Zhao *et al.*[108] incorporated GR modified *N*,*N*′-bis-[2-(ethanoic acid sodium)]-1,4,5,8-naphthalene diimide (NDI) surfactant into nanocrystal SnO_2 ESL. The modification of SnO_2 increased surface hydrophobicity and formed van der Waals interaction between the surfactant and the LHP compounds. The champion device showed a FF of 82% and an accompanying PCE of 20.16%. The stability test showed that GR-based devices maintained more than 90% of their initial PCE after 300 h at room temperature with 30% humidity, whereas the control device PCE dropped to 65%.

Recently, GR was applied in $SrTiO_3/Al_2O_3$–GR ESL for stable and efficient PSCs based on LHP/Ag–RGO light absorber layer.[168] The encapsulated device exhibited notable thermal- and photostability and retained 93% of the initial PCE over 300 d under ambient conditions. The enhancement in the long-term stability was due to the barrier effect of GR sheets, *i.e.*, barrier to moisture penetration and ions migration. Al_2O_3–GR composite acted as both scaffold for LHP layer and charge transport layer due to the presence of conductive GR in the composite. Furthermore, because of less trap state density and recombination in the device based on Al_2O_3–GR composite compared to the device based on mp-TiO_2, it showed substantial improvement in thermal- and photostability.

Following the work by Jeng *et al.*[35] in 2013, different fullerene derivatives have been exploited as ESLs in the planar PSCs. PCBM is one of the most widely used electron extraction and transport material due to its high electron-accepting properties.[7] Moreover, the energy level of the conduction band of PCBM is well-aligned with that of the LHP.

A modification of the fullerene has been performed using a cross-linkable silane containing hydrophobic groups. Using this treatment, penetration of water molecules to the LHP layer was shown to be blocked, resulting in improved stability, with solar cells retaining about 90% of their efficiency after 30 days. The photographs demonstrating the water-resistivity of the devices based on conventional PCBM and the cross-linkable silane-functionalized fullerene are shown in Fig. 7b.[165] A dimeric fullerene derivative (D-C_{60}) with two [6,6]-phenyl-C_{61}-butyric acid methyl ester ($PC_{61}BM$) units (Fig. 7c) has also been used as an ESL in PSCs. The devices based on this ESL showed better stability under a 50% humidity in the air at room temperature. This is attributed to the higher hydrophobicity and the more compact structure of the D-C_{60} layer in comparison to PCBM.

However, the explicit influence of the functional groups of fullerene derivatives on the PSCs' performance and stability is still unclear. Tian *et al.*[169] studied the effect of a branched alkyl chain of a $PC_{61}BM$-like fullerene derivative, [6,6]-phenyl-C_{61} butyric acid 2-ethylhexyl ester ($PC_{61}BEH$), on performance and stability of inverted planar PSCs. Fig. 7d shows the structure of $PC_{61}BEH$. Due to the high solubility of $PC_{61}BEH$ in chlorobenzene, highly homogenous films were formed, which enhanced passivation and improved electron extraction. Additionally, the resulting dense and hydrophobic films of $PC_{61}BEH$-based devices resulted in improved device stabilities when compared with those of $PC_{61}BM$-based devices. The device stabilities were conducted under a 45–50% humidity in air at room temperature without encapsulation. Fig. 7e shows

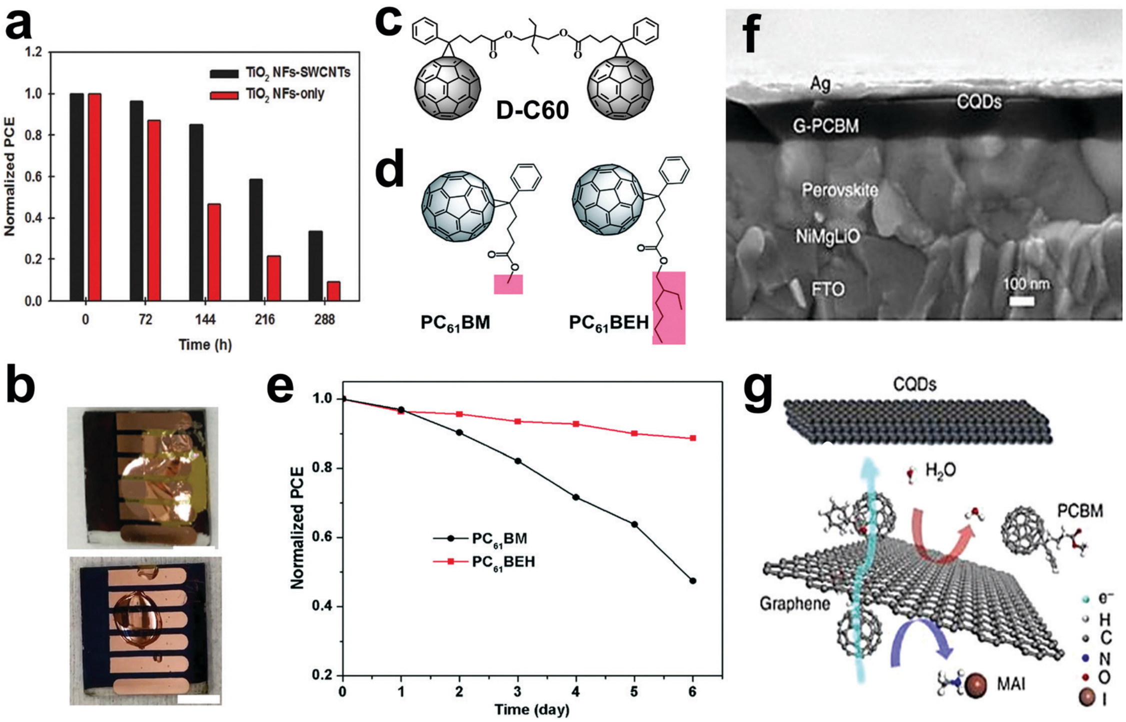

Fig. 7 Stability of PSCs by using carbon-based materials in ESL. (a) Normalized PCE of unencapsulated PSCs with and without SWCNTs in the TiO_2 nanofiber ESLs as a function of storage time. (Solar cells were kept in the dark in ambient conditions at a relative humidity of 60%), reprinted with permission.[161] (b) Photographs of the devices based on ESLs with conventional PCBM (top) and with cross-linked silane-functionalized fullerene (bottom) after exposure to a water droplet for 4 min. The scale bars in both the images are 0.5 cm, reprinted with permission under Creative Commons license.[165] (c) The structure of D-C_{60}, reproduced with permission.[166] (d) Molecular structure of $PC_{61}BEH$ and $PC_{61}BM$. (e) Normalized PCE of PSCs employing $PC_{61}BEH$ and $PC_{61}BM$ as the ESLs as a function of storage time in air. (f) SEM cross-section image of a NiMgLiO/halide LHP/N-doped GR fullerene derivative phenyl-C_{61}-butyric acid methyl ester (G-PCBM)/CQDs/Ag device, where G-PCBM and CQDs stand for GR-doped PCBM and carbon quantum dots, respectively. (g) Schematic drawing of the diffusion processes within the nanocarbon-based ESL, reprinted with permission under the Creative Commons license.[167]

that $PC_{61}BEH$-based devices exhibited better stabilities because of their hydrophobicity and film morphology, resulting from the branched functional group.

There are still numerous concerns in PCBM ESLs, like current leakage, recombination at the interface, and poor surface coverage, which need to be addressed.[170] Hence, doping and chemical modification of the PCBM layers have shown to be an efficient way to achieve better stability of the PSCs. A mixture of PCBM and C_{60} shows better trap passivation and an increase in the conductivity when compared to the pure PCBM.[171]

The stability of inverted PSCs based on different fullerene derivatives, *cis*-dimethoxy carbonyl fulleropyrrolidine C_{70} ($DMEC_{70}$); α-$DMEC_{70}$ isomer, mix-$DMEC_{70}$ (mixture of three different *cis*-$DMEC_{70}$ isomers (α, β-endo, and β-exo)), and $PC_{71}BM$ as the ESL in a relative humidity of ~20% was investigated by Castro and co-workers.[53] The unencapsulated devices with the PSCs based on α-$DMEC_{70}$ showed the highest stability over this period of time. This was attributed to the higher hydrophobicity of this ESL in comparison to the two others, which reduced water intrusion into the LHP layer.

Work by Bi *et al.* has shed light onto other carbon-based materials, which were shown to act not only as ESL but also suppress the detrimental ion/molecule diffusion within PSCs and increase the carrier lifetimes.[167] A nanostructured carbon layer consisting of N-doped GR, PCBM, and carbon quantum dots was used between the LHP layer and the metal electrode in heterojunction PSCs, as shown in a cross-sectional SEM image in Fig. 7f. Iodide diffusion from the LHP absorber layer to the electrode as well as the migration of Ag atoms from the electrode to the LHP layer (which both are the degradation pathways for the PSCs) were hindered by the carbon layer resulting in stable devices. Fig. 7g shows schematic representations of the carbon layer, which blocks the layer-to-layer migration of iodide and water molecules. Stability tests showed that the PCE of the devices remained close to the initial value (15%) during thermal aging at 85 °C for 500 h and light soaking for 1000 h.

ESLs based on carbon-based, particularly fullerene-based derivatives, can be processed at low temperatures, which is compatible with device fabrication on flexible substrates. Despite the intensive research on optimizing the ESLs, it is challenging to improve the durability of the PSCs by ESL engineering.[7]

3.2 Perovskite active layer

The light-harvesting layer is a primary layer in PSCs and the underlying properties of this layer, such as light-harvesting efficiency, morphology, and charge separation efficiency, are crucial factors in PSCs. Improvement of the morphology of the active layer is essential to hinder current leakage and enhance light harvesting.[86] Furthermore, by increasing the grain size, grain boundary concentration in the LHP layer decreases and ion migration is reduced, improving the hysteresis and long-term stability of the devices.[172] LHPs are prone to defect formation on the crystal surface or at the grain boundaries. Passivation of these defects is an efficient approach in order to improve photovoltaic performance.[173]

Carbon-based materials have been incorporated in the LHP light-harvesting layer mostly to improve the morphology,[68,92] decreasing the hysteresis properties,[27] and reducing the charge recombination.[86] However, there are just a few studies reporting the stability improvement by application of carbon-based materials in the LHP active layer. Yavari *et al.*[174] applied carbon nanoparticles containing functional groups to the LHP layer of PSCs. The interaction of functional groups on carbon nanoparticles with LHP components resulted in a larger LHP grain size. This modification on the solar cell, which made the LHP film more hydrophobic and more thermally stable compared to the control device, with little change in the photocurrent. The absorption spectra of the LHP films before and after the heat stress test in dry air (120 °C for 2 h) showed no change in absorption in the presence of carbon nanoparticles, while the control LHP film showed pronounced changes. The presence of the carbon nanoparticles which formed hydrogen bonding between carbon nanoparticles and FA might be the reason for increased thermal stability.

LHPs are prone to defect formation on their surfaces or at the grain boundaries due to anion and cation migration under applied bias.[175] Therefore, the passivation of these defects is an efficient approach to improve photovoltaic performance and stability.[176] Carbon quantum dots were used as additive in the LHP layer in order to passivate the crystal defects, improve the crystallinity, increase the grain size, reduce the grain boundary, and, in general, prepare high-quality $MAPbI_3$ films.[177] The unencapsulted devices with carbon quantum dots additive in LHP maintained 85% of their initial PCE after 20 days in air with humidity of 30% (at 20 °C), while the PCE of PSC with pristine LHP decreased by 44%. Uncoordinated Pb atoms on the surface of LHP films as the main source of charge traps interacted with functional groups of carbon quantum dots such as carboxyl, hydroxyl and amino which reduced the defects on the LHP film.

The hydrophobic properties of carbon-based materials, when incorporated into the LHP layer, can hinder the water diffusion to the layer and increase the stability of the devices. Guo *et al.*[173] used carbon quantum dots as an additive to the $MAPbI_3$ LHP. The hydrophobic carbon quantum dots attached to the LHP surface were shown to block water diffusion into the LHP. It resulted in enhancing the long-term stability of the PSC. The LHP film showed much less degradation under ambient conditions (with humidity of 50–60%) after 300 h, in comparison to the pristine $MAPbI_3$ film.

A molecularly designed graphite-nitrogen doped GQDs (GN-GQDs) was used as a functional semiconductor additive in LHP film by Gan *et al.*[178] In addition to passivating the grain boundary trap states due to the Lewis base/acid interaction, the GN-GQDs exhibited a bandgap with valence band and conduction band matching well with the energy structure of $MAPbI_3$, which accelerated the charge transport. Based on the reduced trap states and more hydrophobic property of LHP film, the device showed better environment stability at ambient under 30% humidity for 30 days without encapsulation.

Incorporation of PMMA–fullerene complex inside the LHP layer resulted in improved performance and stability of PSCs.[179] The fullerene located at the LHP grain boundaries and formed a dipole-like electric field inside the LHP layer. It favored charge carrier separation improving the device performance. PMMA molecules in the complex made it more hydrophobic, which blocked the moisture penetration into the LHP layer. The hybrid LHP showed superior stability against moisture, heat, and light. The PSCs exhibited no photovoltaic performance degradation in ambient air for 250 d under long-term stability testing. Under continuous illumination in ambient air, the PSCs incorporated with PMMA–fullerene show approximately 60 times higher stability than the state-of-the-art PSC.

Although these results confirm that the application of carbon-based materials in the LHP layer provides PSCs with a longer lifetime, there is still room for research focusing on it. Many carbon-based materials are not dispersible in the solvent compatible with LHP. The functionalization of carbon-based materials could be useful for this purpose, providing that their characteristics are not disturbed.

3.3 Hole selective layer

A suitable HSL requires proper electronic properties and a well-matched valence-band energy level to the LHP layer to facilitate an efficient hole extraction. In addition to these properties, HSLs should meet certain requirements such as high-temperature stability, low cost, and, ideally, hydrophobicity. All of these characteristics needs to be taken into account in the commercialization of PSCs.[180] Different materials including either inorganic materials (NiO, CuSCN, MoO_3, and CuI) or organic materials such as 2,2′,7,-7′-tetrakis(*N*,*N*-di-p-methoxyphenylamine)-9,9′-spirobifluorene (spiro-OMeTAD), poly(3-hexylthiophene-2,5-diyl) (P3HT), PTAA (poly(triaryl amine)), and poly(3,4-ethylenedioxythiophene):polystyrene sulfonate (PEDOT:PSS) have been found appropriate as HSLs in PSCs. In addition to the traditional HSLs, carbon-based materials are particularly promising materials for application as HSLs or as additives to the common HSLs in order to improve the hole transport mobility as well as the stability of devices.[122,181–183] Different groups have reported that the performance of devices based on spiro-OMeTAD was improved with the incorporation of CNTs and GR derivatives.[70,72,122]

The HSL plays a critical role in the stability of PSCs, particularly in the traditional device architecture; FTO/n-type/LHP/p-type/metal electrode. The properties of conventional HSLs, such as hydrophobic properties, resistance to ion migration, and thermal stability are factors that affect the stability of the devices.[15,98] A central focus of many studies has been related to the poor barrier properties of common HSLs that cannot hinder moisture ingress. Organic HSLs are usually susceptible to the migration of halide ions and metal ions (from the metal electrode), which inevitably results in device degradation.[147]

The commonly used HSL, spiro-OMeTAD, is unstable in outdoor applications. Spiro-OMeTAD is a poor barrier for the interaction of the metal electrode and LHP due to the severe morphological deformation under thermal stress (formation of large voids). Indeed, spiro-OMeTAD crystalizes at high temperatures creating pathways for the diffusion of metal from the electrode to the LHP.[2,184–186]

Spiro-OMeTAD exhibits low electrical conductivity (9.1×10^{-7} S cm^{-1})[187] in its pristine form and doping it with lithium bis(trifluoromethanesulfonyl)imide (Li-TFSI) to reduce the series resistance, and charge recombination has been shown to be mandatory. Li-TFSI is hygroscopic, which accelerates the moisture-induced degradation of the LHP layer under ambient conditions.[122,185] In addition, Li-TFSI can further reduce the adhesion between the LHP and the HSL resulting in poor ambient stability of the PSC.[122,187,188] Another common additive in spiro-OMeTAD is *tert*-butylpyridine (TBP), which acts as a morphology controller in order to improve the contact between the HSL and the LHP layer, as well as to suppress charge recombination in the device.[122] TBP is a polar solvent of a similar nature as the solvents used for the deposition of the LHP precursor solution. This can lead to the dissolution of the LHP layer. Thus, it is necessary to develop new stable HSLs or more stable additives to replace Li-TFSI and pyridine dopants for the scale-up and commercialization of PSCs.

PEDOT:PSS is a common HSL in inverted planar PSCs due to its tunable conductivity and high optical transmittance. Unfortunately, it is detrimental to the stability of the devices because of its acidic nature.[189–191] Many groups have reported that the stability of the PSCs can be improved by application of the carbon-based materials either by incorporating them in the common HSLs or by applying them as alternatives for HSLs.

3.3.1 Carbon-based additives in hole selective layer.

A thermal stability comparison between LHP films coated with different HSLs, including spiro-OMeTAD, P3HT, PTAA, and SWCNT–PMMA composite, was performed by Habisreutinger *et al.*[65] (Fig. 8a). Signs of degradation of the LHP layer were observed within 24 h, and the degradation progressed considerably within 96 h for LHP films coated with organic HSLs. Interestingly, in the case of spiro-OMeTAD, the degradation is also accelerated in the presence of the highly hygroscopic lithium-based dopant. It confirms the importance of developing nonhygroscopic HSLs, which would prevent moisture from interacting with the LHP film. By using an HSL consisting of hydrophobic polymer poly(methyl methacrylate) (PMMA) mixed with SWCNTs (*i.e.*, an SWCNT–PMMA composite) no significant degradation was observed after 96 h. PMMA acted as a protective layer and shielded the LHP film from moisture. However, because of its insulating characteristics, PMMA is not capable of transporting charge carriers. Owing to exceptional electronic properties, SWCNTs improved the charge transport in this HSL. By wrapping CNTs with a monolayer of P3HT, supramolecular nanohybrids (P3HT/SWNT) were formed and allowed the dispersion of CNTs in

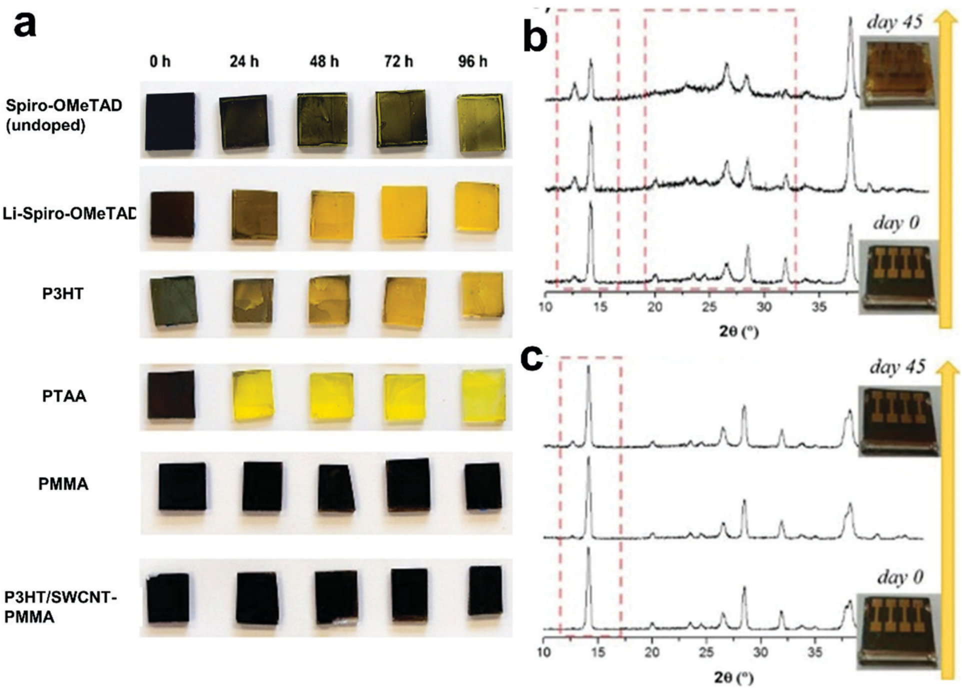

Fig. 8 Carbon-based materials as additives in HSL (a) Optical images of the degradation of the LHP layers with different materials on top of the films, reproduced with permission.[65] (b) XRD patterns of the device based on Li-doped spiro-OMeTAD and (c) XRD pattern of devices based on SWNTs-doped spiro-OMeTAD from 0 to 45 days exposition at ambient conditions (RT, RH = 70%). The combination of the (002)/(110) planes is found at ∼14.1° and that of the (004)/(220) planes at ∼28.4°. The other low-intensity diffraction peaks at ∼23.5°, 31.9°, 40.5°, and 43.20° are assigned to the (211), (312), (224), and (006)/(330) planes. Peaks at 26.5°, 33.8°, and 37.9° are assigned to FTO, reprinted with permission.[192]

a common solvent for spin coating the HSL. Moreover, the P3HT affects the electronic properties and results in a p-type charge collection layer. By replacing the organic hole-transporters with this HSL, PSC with 15.3% PCE was achieved with enhanced thermal and moisture stability.[65] The devices without encapsulation maintained their efficiencies after 96 h exposure to a temperature of 80 °C in air. However, devices with Li-TFSI doped spiro-OMeTAD, P3HT, and PTAA HSLs lost their efficiencies after thermal stress in the air.

Miletić *et al.*[192] showed the improved chemical stability of the LHP is the advantage of the SWCNTs doping of spiro-MeOTAD in comparison to the Li-doped spiro-MeOTAD. The effect of the doping spiro-MeOTAD with chemical functionalized SWCNTs and LiTFSI on the stability of LHP films was compared by continuously exposing them to the environment for 45 days (ambient air, 70% relative humidity and room temperature). The X-ray diffraction (XRD) patterns of the devices with SWCNTs doped spiro-OMeTAD and with the standard Li salt doped spiro-OMeTAD are shown in Fig. 8b. The XRD shows the degradation of the LHP to PbI_2 by the final large amounts of PbI_2 (characteristic (001) peak at 12.65°). The yellowish device color (inset Fig. 8b) also confirmed the PbI_2 formation. The intensity of the $CH_3NH_3PbI_3$ main peak at 14.1° was also extremely reduced after 45 days of exposure. The appearance of a broad background in the 2θ window between 20 and 30° was attributed to the changing of the crystalline LHP phase into an amorphous form. The LHP active layer was severely damaged by moisture and possible migration of Li^+ from the HSL. For the aged devices doped with SWCNTs, instead, the PbI_2 peak was significantly smaller, and the LHP XRD peaks maintained the same shape and intensity, showing a minor degree of decomposition (Fig. 8c). The improved moisture resistance demonstrates the suitability of this material as a valid doping agent for spiro-MeOTAD as an alternative to the conventional Li salt.

Carbon-based materials have been used as HSLs in PSCs to replace the detrimental additives of spiro-OMeTAD and to enhance the stability of PSC. Solution-processable GO reduced by ferrous iodide acid solution was used together with dopant-free spiro-OMeTAD in a mesoscopic device architecture by Luo *et al.*[122] In their work, the hole transporting layer was prepared by first spin-coating the RGO dispersion and subsequently spiro-OMeTAD. Although the reference solar cell showed better performance, the devices with RGO showed improved stability in ambient conditions, *i.e.*, only a 15% PCE degradation after 500 h with a maximum PCE of 10.6%. However, the PCE of the device with Li-TFSI and pyridine doped spiro-OMeTAD HSL dropped by 65% in the same timeframe.

NiO_x as a p-type semiconductor with low-temperature processing is typically used in inverted PSCs, particularly flexible devices.[193,194] However, the band alignment between low-temperature-processed NiO_x and the LHP layer is not adequate, resulting in reduced photovoltaic performance. Carbon-based materials have been applied in HSL based on NiO_x. Amino-functionalized GQDs (AGQDs) were used in NiO_x HSL for optimizing the band structure alignment between the NiO_x and LHP layer to facilitate the hole extraction at the NiO_x/LHP interface. In addition to the improvement of performance, the device showed good air stability and mechanical stability.[194]

3.3.2 Hole selective layers based on carbon materials. GR-based materials have been widely used as HSLs in PSCs. In an early study, a functionalized nano GR (perthiolated trisulfurannulated hexa-*peri*-hexabenzocoronene, TSHBC) was used as the HSL to improve the stability of mesoscopic $MAPbI_3$ PSCs.[195] The structure of TSHBC is shown in Fig. 9a. The formation of a Pb–S coordination bond between the LHP absorber and TSHBC contributed to an efficient electron extraction at the interface. A PCE of 12.8% was reached by using TSHBC as the HSL, which was further improved to 14% by doping TSHBC with GR sheets (because of better charge transfer). The hydrophobic nature of both TSHBC and TSHBC/GR layers allowed them to adequately protect the LHP layer resulting in more stable devices in comparison to spiro-OMeTAD. Fig. 9b shows that the contact angle of water droplets on TSHBC as well as TSHBC/GR were 107°, while the contact angle on spiro-OMeTAD was only 80°. The devices with spiro-OMeTAD lost ~80% of their efficiency after 10 days, while the cells with TSHBC and TSHBC/GR retained 85% and 90% of their original PCE over 10 days under the same storage condition, respectively. Under illumination, the efficiency of devices with spiro-OMeTAD reduced to 25% within 60 min. However, devices with TSHBC retained 60%, and the cell with TSHBC/GR showed 70% of the original efficiency after 400 min. The rapid drop in PCE was ascribed to the intrinsic thermal instability under illumination.

The high potential of GR-based HSLs for efficient and stable PSCs was further confirmed by using a composite consisting of GR and functionalized CNTs (GR: f-CNTs) as an efficient HSL in PSCs with good conductivity and hole mobility.[190] The GR: f-CNT composite, which is prepared by π–π interaction between the GR sheets and the functional CNTs, acted as a scaffold for LHP crystallization and enhanced the stability of the devices without encapsulation. The devices with a PEDOT:PSS HSL showed a 70% decrease in the efficiency after 48 h, while the PCE of the devices with GR: f-CNT composite decreased by 20% (temperature 35 °C, humidity 20%) in 48 h, Fig. 9c. The improved stability was ascribed to the hydrophobicity and neutral charge of the composite. A new transfer method by a vacuum lamination process was developed by Ishikawa *et al.* in order to use GR as an HSL.[196] Vacuum lamination is a process that binds the layers together under pressure and vacuum. Although the device based on GR HSL showed lower efficiency, it had better stability in comparison to spiro-OMeTAD devices. This is suggested to be due to the GR layer blocking the humidity and oxygen diffusion to the LHP absorber layer.

GO is a stable material and does not react with the LHP layer in PSCs.[98] In comparison to conventional PEDOT:PSS, the GO-based devices displayed an enhancement in stability. They maintained more than 90% of the initial PCE after 2000 h, while The PCE of the PEDOT:PSS-based device decreased to 40% of the initial PCE after just 1400 h over a long-term storage/operation.[98] The *J*–*V* curves of encapsulated devices with PEDOT:PSS and GO-based HSL for 78 days over cycles of

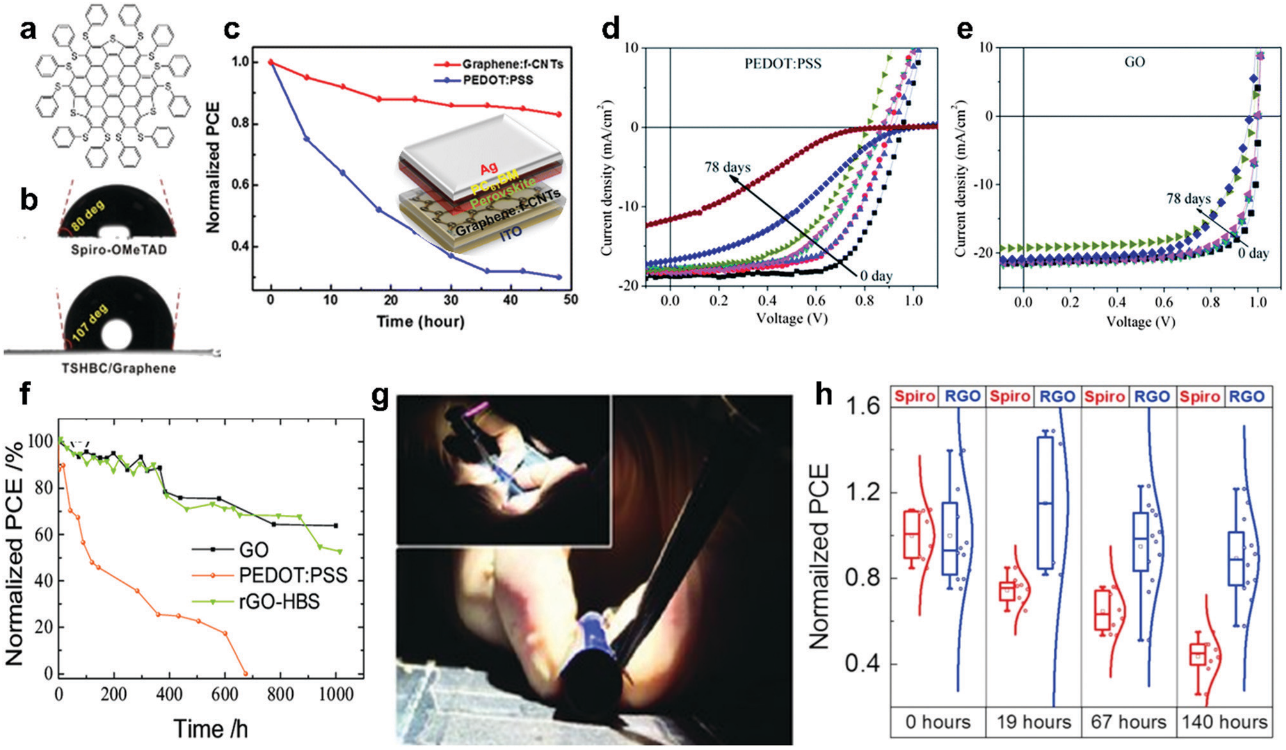

Fig. 9 Effect of carbon-based materials used as HSL on the stability of PSCs. (a) Structure of TSHBC. (b) The water contact angles on spiro-OMeTAD and TSHBC/GR, reprinted with permission.[195] (c) Normalized PCEs of PSCs based on Gr-CNTs and PEDOT:PSS HSLs as a function of storage time in ambient air, reprinted with permission.[190] J–V curves of (d) PEDOT:PSS- and (e) GO-based devices at 0 to 78 days, reprinted with permission.[98] (f) The stability of devices with PEDOT:PSS, GO, and rGO-HBS HSLs as a function of storage time (at 25 °C and humidity of 30% with no encapsulation). (g) Bending experiments on flexible devices based on ITO/PEN substrates and RGO HSLs, reprinted with permission.[123] (h) Normalized PCE of devices with spiro-OMeTAD and RGO HSLs deposited by 20 cycles of spray coating, reprinted with permission.[188]

operation/storage conditions are shown in Fig. 9d and e. The V_{OC} remained almost unchanged during these storage and operation tests. The reason for rapid decrease in PCE of the devices based on PEDOT:PSS is the sensitivity of organic PEDOT:PSS to oxygen and moisture. Moreover high acidity and hygroscopic properties of PEDOT:PSS cause detrimental effects in device stability.[98]

The hole conductivity of GO is increased by reducing it (although still lower than that of pristine GR).[188] The solubility, conductivity, and surface chemistry of RGO are controlled by the reduction procedure and the reducing agent.[180] RGO fulfills almost all of the necessities of a relatively ideal HSL, including ease of fabrication, low cost, high conductivity, and high stability. Solution-processed RGO has been exploited as HSL in direct and inverted PSCs by focusing on the stability issues of the devices.[99] Yeo *et al.*[99] reported the application of a facile solution-processed RGO as an HSL in inverted PSCs with the configuration of glass/ITO/RGO/$CH_3NH_3PbI_3$/$PC_{61}BM$/bathocuproine(BCP)/Ag. The devices showed enhanced stability in comparison to devices based on PEDOT:PSS HSL (in 50% humidity). Devices based on the RGO HSL retained around 62% of its PCE after 140 h. The performance of the devices with the PEDOT:PSS HSL showed a significant drop after 120 h.

The higher stability of GO and RGO HSLs relative to PEDOT:PSS in planar PSCs was further confirmed by Jokar *et al.*[123] As shown in Fig. 9f, devices with HSLs based on GO and RGO reduced by 4-hydrazino benzenesulfonic acid (RGO-HBS) maintained half of their initial efficiencies after 1000 h storage. However, the device with PEDOT:PSS HSL completely stopped working within 650 h. Furthermore, the flexible PSCs using RGO as HSL on a flexible ITO/PEN substrate maintained 70% of their initial performance after 150 mechanical bending cycles, Fig. 9g.

Enhancing the stability of PSCs by employing RGO as the HSL in n–i–p configuration was also investigated by Palma *et al.*[188] by spray-coating a suspension of RGO on top of the LHP layer. The RGO alternative to spiro-OMeTAD showed a PCE 40% lower than the control, which was attributed to poor coverage on the LHP surface. However, the devices based on RGO HSL showed superior stability (ISOS-D-1 shelf-life aging test).[197] The unsealed PSCs were kept in the dark and air with 50% humidity under open-circuit conditions. A 138 h shelf-life test showed the devices based on the RGO HSL lost 11% of their initial PCE, whereas the efficiency of the devices based on spiro-OMeTAD HSL was reduced by over 55%, Fig. 9h.

Some HSLs do not meet the requirements of an efficient PSCs while other materials, such as spiro-OMeTAD, have been used in highly-efficient PSCs. However, the need for detrimental additives in these HSLs may cause severe stability issues in the real application of the PSCs. Therefore, replacing

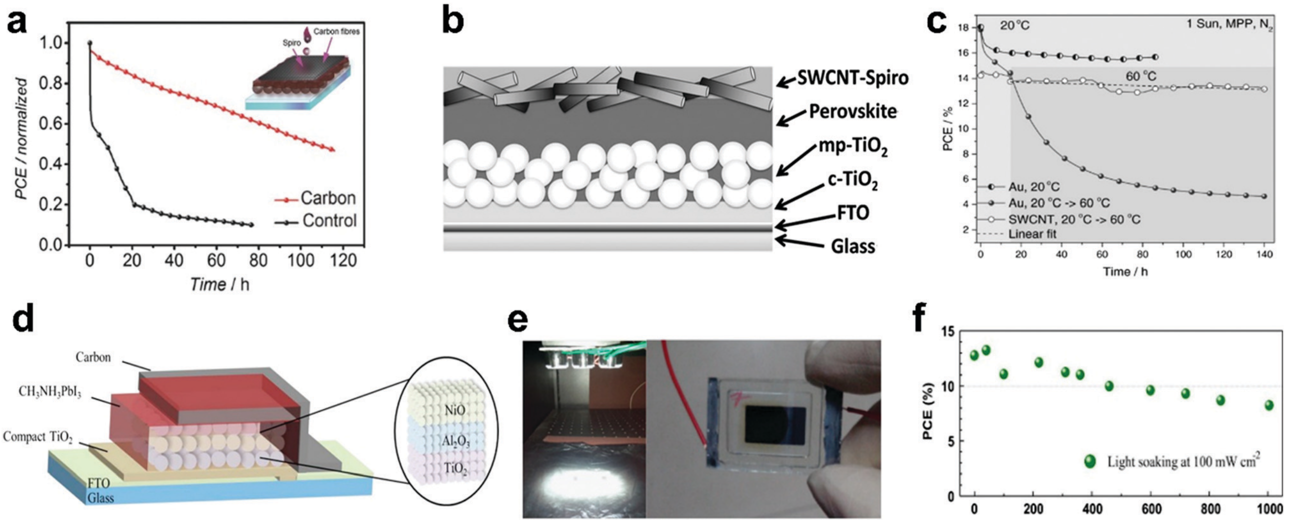

Fig. 10 Stability of PSCs based carbon electrodes. (a) MPP tracking under constant illumination for carbon-based (carbon cloth embedded in carbon paste/spiro-OMeTAD) and control (spiro-OMeTAD/Au) device in the nitrogen atmosphere at 85 °C, reproduced with permission.[205] (b) Schematics of the SWCNT-contacted device. (c) MPP tracking of the devices with Au and SWCNT back contact at 60 °C, reprinted with permission.[203] (d) The device structure of the $TiO_2/Al_2O_3/NiO$/carbon ($MAPbI_3$)-based device. (e) Light soaking test at 100 mW cm^{-2} (with white light emitting diodes) and a photograph of the sealed device. (f) Stability investigation of the devices with $TiO_2/Al_2O_3/NiO$/carbon ($MAPbI_3$) structure during the light soaking test, reprinted with permission.[201]

HSLs or their additives is an efficient approach in increasing the stability of the PSCs while preserving efficiency. Due to their high operational stability and lower cost in comparison to the commonly used HSL, the carbon-based HSLs show great potential in the commercialization of PSC technologies both as HSL and as additives to HSLs. However, a systematic investigation of the stability of the PSCs with carbon-based HSLs for enhancing long-term stability is still required.

3.4 Electrode

3.4.1 Carbon materials for replacing the metal electrode. The electrodes in the state-of-the-art PSCs typically consist of expensive metals such as Au or Ag. Metal migration into the LHP layer and degradation of the metal contact are important degradation pathways in PSCs, which in turn severely affect the long-term stability of the devices.[186,198,199] The degradation of PSCs due to the metal back contact under working conditions has been overcome to some extent by replacing the metal-based electrodes with designing various novel cathodes based on low-cost and abundantly available carbon-based materials. Carbon materials have several advantages such as an aligned work function, facile and low-cost fabrication, mechanical flexibility, and, most importantly, high stability.[148,200]

In 2013, Ku *et al.*[134] pioneered the application of low-cost and stable carbon electrodes for replacing the metal contact in PSCs. Subsequently, many studies have applied carbon back contact electrodes in PSCs in order to achieve long-term stable PSCs. Many carbon materials including graphite, carbon black,[201] spongy carbon,[202] CNTs,[203] coal powder,[204] and Carbon cloth[205] have been used as the electrode in PSCs. Gholipour *et al.*[205] exploited carbon cloth embedded in carbon paste as the electrode. This electrode improved the long-term stability of the devices in comparison to gold electrodes under elevated temperatures. Fig. 10a shows the stability of the devices with carbon cloth and gold back contact (control) at 85 °C by maximum power point (MPP) tracking. At 85 °C, the device with the carbon cloth electrode retained more than half of the initial PCE after 100 h, while the control device efficiency decreased to less than 10% after 65 h. The rapid degradation of the Au device was ascribed to the metal/LHP interactions, which was avoided by the use of the carbon electrode.

It has been shown that CNT films can increase the stability of PSCs when substituting the metal electrode. Aitola *et al.*[203] enhanced the stability of PSCs by combining spiro-OMeTAD and SWCNT films as HSL and electrode. The configuration is shown in Fig. 10b. MPP tracking data of the Au and SWCNT-contacted devices under white light-emitting diode (LED) illumination for 140 h with an intensity equivalent to 1 sun was collected (Fig. 10c). By conducting the experiment at 60 °C in N_2 atmosphere, the device with the SWCNT cathode exhibited minimal efficiency loss, while the efficiency of the device with the metal back contact was reduced dramatically under MPP tracking. It has been reported that Au-induced degradation of the LHP layer results in loss of photovoltaic parameters.[186] The slight decrease in photovoltaic performance of the devices based on SWCNTs could be due to the slow degradation of LHP film due to the residual water or oxygen, LHP phase transition, light induced trap states, and ionic movement.

In addition to the commonly reported PSC device structure, carbon electrodes have also been used in other PSC configurations. For instance, they have been used in the architectures which are entirely constructed of inorganic metal oxides ($TiO_2/Al_2O_3/NiO$/carbon ($MAPbI_3$)). The configuration is a quadruple layer of mesoscopic $TiO_2/Al_2O_3/NiO$/carbon used as the scaffold, which is infiltrated with $MAPbI_3$ shown in Fig. 10d.[201,206] Cao *et al.*[201] performed stability tests on the TiO_2/Al_2O_3/NiO/carbon ($MAPbI_3$) devices. The devices retained over 80% of the PCE after 1000 h at 60 °C in the dark. Moreover, the stability of sealed devices were subjected to a constant light soaking under ambient atmosphere at room temperature with relative humidity of 40% (Fig. 10e). The stability results shown in Fig. 10f indicates that the devices maintained 82% of the initial PCE after 500 h. Xu *et al.*[206] also showed that the PSCs with this structure maintained over 93% of its initial values when stored under ambient conditions with about 40% humidity for 1000 h (in dark). However, under light, temperature of 45 °C, and 40% humidity, the stability was an issue for the devices and the PCE decreased by about 80% of the initial value after 150 h. The stability of PSCs using carbon electrode is due to the protection by the thick carbon layer back contact.[201] Carbon does not affect the LHP layer by ion migration which typically occurs in PSCs based on Au contact.

Applications of carbon-based materials as the electrodes in PSCs not only provide solar cells at a lower cost and high stability but it also offers PSCs with more features such as flexibility and semi-transparency with dual side illumination, which can be used in perovskite–perovskite tandem solar cells connected in series.

3.4.2 Hole selective layer-free perovskite solar cells with carbon electrodes. In addition to the importance of contact in the stability of PSCs, especially at high temperatures, the organic HSLs are mostly unstable and allow the metals from the electrodes to interact with the LHP layer resulting in unstable devices. On the other hand, apart from its function as a photoabsorber, the LHP layer is able to transport holes and electrons efficiently, making it possible to fabricate HSL-free devices. Various types of HSL-free PSCs have been explored by applying Au or carbon hole-extraction electrodes. Amongst them, the application of stable and water-resistant carbon electrodes is an elegant solution for the stability issues.[17] Carbon electrodes are chemically stable, inert to ion migration, and moisture resistance making them the promising conducting electrode.[207] Many groups have explored the stability of the HSL-free PSCs using carbon electrodes (C-PSCs) and considerably high stabilities have been reported for this type of PSCs.[139,150,208,209]

C-PSCs usually have the architecture of FTO/TiO_2 dense layer/TiO_2 mesoporous layer/LHP/carbon (Fig. 6). Ku *et al.*[134] fabricated mesoscopic C-PSC with a carbon black/spheroidal graphite counter electrode (achieving 6.6% PCE) with almost no performance decay in 840 h in dry air at room temperature and without encapsulation.

Mei *et al.*[139] fabricated fully printable C-PSCs by drop-casting a solution of PbI_2, methylammonium iodide, and 5-ammoniumvaleric acid (5-AVA) iodide through a porous carbon film. The device with mixed-cation LHP $(5\text{-AVA})_x(MA)_{1-x}PbI_3$ showed a certified PCE of 12.8%. The crystals of $(5\text{-AVA})_x(MA)_{1-x}PbI_3$ in this fully printable mesoscopic C-PSC had fewer defects and better contact with the TiO_2 scaffold. The non-encapsulated devices retained their initial performance for over 1000 h in an air atmosphere under solar irradiation.[139]

The hydrophobic properties of the carbon-based electrodes were investigated by Yu *et al.*[210] C-PSCs retained 98% and 92% of their initial efficiencies when they were exposed to water flushing and water immersing, respectively (Fig. 11a).

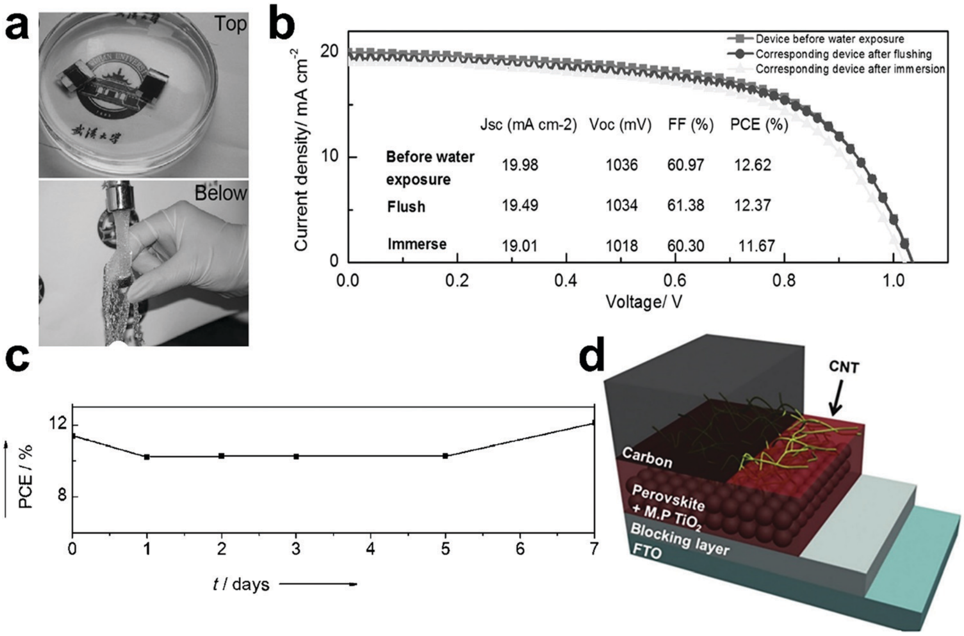

Fig. 11 Stability of C-PSCs. (a) A photo of a PSC immersed in water (top) and placed under running water (bottom). (Encapsulated devices were exposed to running water for 30 s and immersed in water for 15 min). (b) *J–V* curves of an as-prepared solar cell before and after water exposure, reprinted with permission.[210] (c) The outdoor stability test of encapsulated C-PSCs in Jeddah, Saudi Arabia, reprinted with permission.[139] (d) Schematic illustration of C-PSC based on the CNT dripping method, reprinted with permission.[211]

Fig. 11b shows the *J–V* curves of the devices, which were almost unchanged before and after water exposure. The devices were also stable under thermal stress at 150 °C for 30 min. The improvement in moisture stability is due to the hydrophobic nature of carbon, which protected the LHP from degradation during the water permeation and removing the hydroscopic dopants (Li-bis(trifluoromethanesulfony)-imide) typically used in the spiro-OMeTAD.

A C-PSC has outstanding stability under different conditions. Zhou *et al.*[148] fabricated devices with the long-term durability of over 2000 h in air and dark (for non-encapsulated devices). An outdoor stability measurement of C-PSCs based on a triple layer structure was conducted by Li *et al.*[212] in a hot desert climate in Jeddah, Saudi Arabia. The test showed that the photovoltaic parameters were stable for seven days under the hot and humid climate conditions highlighting the strong resilience of the devices, Fig. 11c. The stability tests under indoor light soaking and prolonged heat stress (80–85 °C) for encapsulated PSCs for three months showed almost no change in the device performance.

The thermal stability evaluation of a printable three-layer C-PSC based on a $CH_3NH_3PbI_3$ LHP was conducted by Baranwal *et al.*[199] Virtually no PCE loss was shown for encapsulated meso C-PSCs in ambient air at 100 °C for more than 1500 h. The reason for the high thermal stability of C-PSCs is that carbon-based electrodes are inert to ion migration. Conversely, in PSCs with typical HSL and metal contact, temperature of 70 °C is enough to cause migration of metal into the LHP material through the HSL, which in turn severely affects the device performance under working conditions.[186] Many researchers have reported the long-term stability of C-PSCs. Table 2 shows an overview of the reported values on the long-term stability of C-PSCs.

Although there are many reports showing the C-PSCs are promising candidate for stable PSCs, C-PSCs suffer from poor contact at the LHP/carbon electrode interface resulting in a significant amount of undesired charge recombination.[238] To get a seamless interface and better contact between LHP and carbon layer, Ryu *et al.*[211] modified solvent engineering method by dripping off the CNTs dispersed in chlorobenzene solution. This method resulted in the penetration of CNTs into both the LHP film and the carbon electrode, as shown in Fig. 11d. It enhanced the quality of the LHP/carbon interface, particularly because the CNTs aligned upward and facilitated fast hole transport between the two layers. The resulting devices enhanced performance and improved resistance to water ingress into the LHP. The moisture stability of the resultant devices was compared with devices based on spiro-OMeTAD with dopants as HSL and Au electrode. The non-encapsulated C-PSCs maintained $>80\%$ of their initial PCE after 2 h at 30 °C under 50% humidity, followed by 2 h under 80% humidity, while the control devices only maintained 20% of their initial PCE.

The stability of the C-PSCs can be further improved by modification of the carbon electrodes or by employing a more stable LHP absorber. Wei *et al.* enhanced the stability of the carbon electrodes using epoxy, which is a common polymer in carbon paint, and further with an Ag coating.[239] Epoxy is a water-resistant polymer which makes the carbon electrode more hydrophobic. The hydrophobicity of the electrode was further increased by coating the electrode with Ag paint, which also increased the electrode's conductivity. The non-encapsulated C-PSC with epoxy in the carbon electrode showed superior stability (almost unchanged PCE for 20 days), which was further enhanced by the Ag coating at ambient atmosphere (60–80% humidity). A stable C-PSC was developed by Chang *et al.* using an inorganic LHP light absorber ($CsPbBr_3$), which is normally more stable than organic LHPs, together with a painted carbon electrode. The device fabrication was performed under ambient conditions and showed 11.7% loss in efficiency after 250 h at 80 °C.[227] Grancini *et al.*[226] developed a one-year stable PSC by engineering the LHP composition where $HOOC(CH_2)_4NH_3)_2PbI_4/CH_3NH_3PbI_3$ was used as the absorber in a C-PSC architecture. It worth note that the LHP in these C-PSCs is 2D/3D LHP which is more stable than conventional 3D counterparts. The devices were stable for more than 10 000 h (>400 days) in the presence of oxygen and moisture.

Despite their high efficiency, typical PSCs are vulnerable to moisture due to both the hygroscopic nature of dopants (Li-bis(trifluoromethanesulfonyl)-imide) in the HSLs and degradation of the LHP. C-PSC showed strong moisture stability even at 90% RH or higher due to the hydrophobic property of carbon, which prevented degradation of LHP by water penetration into the device. These promising results prove the feasibility and potential of C-PSCs toward stable PSCs. The development of more durable C-PSCs (which is still improving progressively) has brought to light the opportunity to scale-up and commercialization. However, due to poor contact at the LHP/carbon electrode interface and fabrication technique limitations, a significant amount of undesired charge recombination occurs in these HSL-free C-PSCs. Work is still needed to develop C-PSCs with high PCEs and long-term durability comparable to silicon solar cells.

3.4.3 Towards flexible perovskite solar cells.

Flexible PSCs provide portable energy for ubiquitous electronic devices using the advantageous features of PSCs such as high efficiency, low cost, and lightweight.[240] The mechanical stability of electrodes is an essential factor in flexible solar cells. The superior mechanical property of GR and other carbon electrodes make them the perfect candidates as the electrode materials in the flexible PSCs.[241]

The carbon electrode fabricated on flexible polyimide substrate showed good connectivity and mechanical properties (Fig. 12a).[148] Later on, a flexible C-PSC with a structure of $ZnO/CH_3NH_3PbI_3$/carbon on flexible polymer substrates was prepared.[216] Bending test was done on the device by bending it around a pen with 1 cm diameter (Fig. 12b). The stability measurement showed that the flexible C-PSC maintained 80% of the initial efficiency for more than 1000 cycles of bending, as shown in Fig. 12c.

Yoon *et al.* fabricated flexible PSCs using GR as a transparent electrode with the architecture of (PEDOT:PSS/Gr-Mo/PEN) through transferring MoO_x-functionalized GR film on PEN

Table 2 Overview of literature values on the long-term stability of C-PSCs, including relevant parameters such as relative heat, humidity, and illumination. The figures of merit are the total decrease in efficiency and the duration of preserving the performance

Electrode material$^{ref.}$	Device structure	Initial PCE (%)	Light	T (°C)	Sealing	Time (h)	Atmosphere	RH (%)	Total decrease (%)
Carbon black/graphite[139]	FTO/c-TiO$_2$^{a}/mp-TiO$_2$^{b}/ZrO$_2$/(5-AVA)$_x$(MA)$_{1-x}$PbI$_3$/C^c	12.8	AM1.5 G, 100 mW cm^{-2}	RT	No	1008	Ambient	—	Slight increase
Carbon black/graphite[212]	FTO/c-TiO$_2$/mp-TiO$_2$/ZrO$_2$/(5-AVA)$_x$(MA)$_{1-x}$PbI$_3$/C	~10	Dark	80–85	Yes	2160	Oven	—	~7
			Natural light	100	Yes	168	Outdoor	—	Slight increase
			100 mW cm^{-2}	45	No	1056	Argon	—	~0
Carbon paste (carbon/graphite/TiO$_2$/hydroxyl propylcellulose/A-terpinol)[199]	FTO/c-TiO$_2$/mp-TiO$_2$/ZrO$_2$/MAPbI$_3$/C		Dark	100	Yes	1500	Ambient		~0
Carbon black/spheroidal graphite (carbon paste)[134]	FTO/c-TiO$_2$/mp-TiO$_2$/MAPbI$_3$/C	6.64	Dark	RT		840	Dry air		~0
Nano carbon[213]	FTO/c-TiO$_2$/MAPbI$_3$/C	11.6	Dark	25	No	288	Ambient	30	10
Commercial carbon paste[214]	FTO/c-TiO$_2$/mp-TiO$_2$/MAPbI$_3$/C	7.31	1 sun	RT	No	800	Ambient	—	7.42% increase
Commercial conductive carbon paste[148]	FTO/c-TiO$_2$/mp-TiO$_2$/MAPbI$_3$/C	5.89	Dark	RT	No	2446	Air	70	10
Carbon paste (carbon black/graphite[139]	FTO/c-TiO$_2$/mp-TiO$_2$/MAPbI$_3$/ZrO$_2$/C	12.84	AM1.5 G, 100 mW cm^{-2}	RT	No	1008	Ambient		Slight increase
Graphite flake/carbon black powder (carbon paste)[215]	FTO/c-TiO$_2$/mp-TiO$_2$/MAPbI$_3$/C/Al foil	13.53	Dark	RT	No	480	Ambient	—	5
Conductive carbon paste[216]	ITO/PEN/ZnO/MAPbI$_3$/C	4	AM1.5 G, 100 mW cm^{-2}	RT	No	20.8	Air	30	<20
Commercial carbon paste[150]	FTO/c-TiO$_2$/mp-TiO$_2$/MAPbI$_3$/doped-TPDI^d/C	14.9	Natural light	26 ± 5	No	720	Ambient	42 ± 12	17.4
Carbon paste (graphite flake/graphite powder/carbon black/ZrO$_2$[217]	FTO/c-TiO$_2$/mp-TiO$_2$/MAPbI$_3$/C	6.21	Dark	RT	No	1500	Ambient	20	~78
	FTO/c-TiO$_2$/meso-TiO$_2$/MAPbI$_3$/C/PDMS	8.61	Dark	RT	Yes	3000	Ambient	20	Increased to 9.38
Carbon paste (carbon black/graphite)[218]	FTO/c-TiO$_2$/mp-TiO$_2$/MAPbI$_3$/Al$_2$O$_3$/C	12–13	Dark	25	No	5000	Ambient		12% increase
			Dark	70	No	400			10
			1 sun	70	No	240			100
			1 sun	25	No	480			92
Carbon paste (graphite flake, nanographite powder, and carbon black)[219]	FTO/c-TiO$_2$/mp-TiO$_2$/MAPbI$_3$/C	6.21	Dark	20	No	2000	Ambient	20	~40
Carbon paste (carbon black/graphite)[220]	FTO/c-TiO$_2$/mp-TiO$_2$/MAPbI$_3$/C	7.29	Dark	RT	No	240	Air		~0
Conductive carbon ink[221]	FTO/c-TiO$_2$/mp-TiO$_2$/MAPbI$_3$/C	11.44	Dark	RT	No	2880	Dry cabinet without nitrogen	10	~30
Carbon paste[222]	FTO/c-TiO$_2$/mp-TiO$_2$/MAPbI$_3$/Al$_2$O$_3$/C	13–14	Dark	25	No	3000		50	~0
			Dark	70	No	1000	—	50	~60
			1 sun	25	No	200		50	~75
Carbon paste[223]	FTO/c-TiO$_2$/Ag/mp-TiO$_2$/MAPbI$_3$/ZrO$_2$/C	6.7	full sun light	35	No	1046			~0
Carbon paste (graphite and carbon black)[224]	FTO/c-TiO$_2$/mp-TiO$_2$/MAPbI$_3$/mp-ZrO$_2$/C	7.26	Dark	RT	No	1000	Air	70-90	Increased to 9.48
Carbon paste[225]	FTO/c-TiO$_2$/mp-TiO$_2$/MAPbI$_3$/BPC^e	6.78	Dark	RT	No	720	Ambient		~40
Carbon paste[153]	FTO/c-TiO$_2$/mp-TiO$_2$/ZrO$_2$/MAPbI$_3$/C	15.6	Dark	RT	No	3120	Ambient	35	3.3
Carbon black/graphite[226]	FTO/c-TiO$_2$/mp-TiO$_2$/ZrO$_2$/(HOOC(CH$_2$)$_4$-NH$_3$)$_2$PbI$_4$/MAPbI$_3$/C	~12	1 sun AM1.5 G	55	Yes	10,000	Ambient	—	0
Commercial carbon paste[145]	FTO/c-TiO$_2$/mp-TiO$_2$/MAPbBr$_3$/C	8.09	Dark	25-30	No	2160	Dry air	10–20	~0
			Dark	80	No	720	Air	50–85	~20
Commercial carbon paste (carbon black/graphite)[227]	FTO/c-TiO$_2$/mp-TiO$_2$/CsPbI$_3$/C	5	Dark	80		250	Ambient	30–50	11.7
Graphite paste[228]	FTO/c-TiO$_2$/mp-TiO$_2$/MAPbICl$_2$/C	10.3	Ambient	RT	No	240	Ambient	—	~0
Carbon paste[146]	FTO/c-TiO$_2$/mp-TiO$_2$/MAPbI$_3$/C	10.19	—	25	No	720	Ambient	30	2
Carbon paste (carbon black/graphite)[229]	FTO/c-TiO$_2$/mp-TiO$_2$/Al$_2$O$_3$/MAPbI$_2$Br/C	11	25 mW cm^{-2}	RT	No	300	Ambient	50	Increase

Table 2 (*continued*)

Electrode material^ref.^	Device structure	Initial PCE (%)	Light	T (°C)	Sealing	Time (h)	Atmosphere	RH (%)	Total decrease (%)
Cross-stacked superaligned CNTs[230]	FTO/c-TiO_2/mp-TiO_2/$MAPbI_3$/Al_2O_3/CSCNTs[f]/PMMA	~10	Dark	45	Yes	1500	Air	75	17
	FTO/c-TiO_2/mp-TiO_2/$MAPbI_3$/Al_2O_3/CNT		Dark	45	No	1500	Ambient	75	42
	FTO/c-TiO_2/mp-TiO_2/$MAPbI_3$/Al_2O_3/CNT/PMMA		100 mW cm^{-2}	RT	Yes	400	Ambient	39 ± 7	13
	FTO/c-TiO_2/mp-TiO_2/$MAPbI_3$/Al_2O_3/CNT		100 mW cm^{-2}	RT	No	400	Ambient	39 ± 7	54
Commercial carbon paste[231]	FTO/c-TiO_2/mp-TiO_2/$Cs_{0.95}Na_{0.05}PbI_3$/C	10.7	—	20–35	No	1680	Dry air	10–20	0
Boron doped MW-CNTs[232]	FTO/c-TiO_2/mp-TiO_2/$MAPbI_3$/Al_2O_3/B-doped MWNT	15	Dark	RT	No	1920	Dry air	Dry	2
			Dark	80	No	336	Dry air	Dry	15
			Dark	25	No	336	—	65	7
Commercial carbon ink[233]	FTO/c-TiO_2/mp-TiO_2/ZrO_2/MAI:NH_4Cl/C	7.68	—	—	No	576	Air	45	4
Commercial carbon slurry[138]	FTO/c-TiO_2/mp-TiO_2 (anatase@rutile)/$MAPbI_3$/C	15.21	Dark	RT	No	4800	Dry box	20–30	8
Carbon paste[234]	ITO/SnO_2/$CsPbI_2Br$/PMMA/C	10.89		20–25		480	Air	25–35	5
CNT[235]	FTO/c-TiO_2/$PbTiO_2$/$MAPbI_3$/CNT		Dark	25	No	2160	Air	20	5
						960		70	30
Carbon paste[236]	FTO/c-TiO_2/mp-TiO_2/$Cs_{0.05}(MA_{0.7}FA_{0.3})_{0.95}PbI_3$/C	14	—	80	No	100	Ambient	50	10
			—	30	No	240	Ambient	50	~0
Carbon paste[237]	FTO/c-TiO_2/mp-TiO_2/$Cs_{0.05}MA_{0.95}PbI_3$/C	10.57	—	—	No	1000	Ambient	50	10

[a] TiO_2 campact layer. [b] Mesoporous TiO_2. [c] Carbon electrode. [d] 5,10,15-Triphenyl-5*H*-diindolo[3,2-*a*:3′,2′-*c*] carbazole. [e] Boron and phosphorus co-doped carbon. [f] Cross-stacked CNTs.

substrate. The structure of GR-based flexible PSCs is illustrated in Fig. 12d.[104] The device showed 16.8% PCE, and the reference device with (PEDOT:PSS/ITO/PEN) architecture using ITO cathode and PEN substrate showed 17.3%. The flexible devices maintained >90% of its original efficiency after 1000 bending cycles at a bending radius of 4 mm, as shown in Fig. 12e, and 85% of the efficiency even after 5000 bending cycles with a bending radius of 2 mm. However, Owing to the occurrence of the fracture in the ITO layer after bending, the PCE of the PEDOT:PSS/ITO/PEN device failed significantly from 17.3% to 4.3% (Fig. 12e). This overwhelming bending stability highlights that perovskite photovoltaics with carbon electrodes can pave the way for rollable and foldable photovoltaic applications.

3.5 Interfaces between the layers

The weak chemical bonds in the crystal lattice of LHP including ionic bonds, hydrogen bonds, and van der Waals interactions promote LHP decomposition and low stability.[156,242] Typically, the decomposition of LHP starts at the surface which leads to instability of the heterostructures on the surfaces.[156] Many reports have shown that LHP components penetrate through the ESLs and HSLs.[243,244] Due to the low energy barriers to ionic transport in LHPs, the ionic migration is a suspected reason for instability of PSCs.[244,245] It has been reported that metal from the metal contact diffuses to LHP through the HSL.[186,246] Several strategies have been explored to hinder the metal-migration-induced degradation of PSCs.[247] Moreover, ion migration from LHP to the metal electrode through HSL which is accelerated by positive bias and under constant light illumination results in severe irreversible PCE drop.[246]

Interfacial modification has been done in different thin-film photovoltaic cells.[114,248] In PSCs, engineering of the interface between different layers of the device, including the interface between the LHP film and ESL (metal oxides or other organics in planar PSCs or scaffold layer in mesoporous devices), LHP layer and HSL, and HSL and metal contact is critical for long-term stability of devices.

Trap states the surface may lead to various challenges, such as recombination loss and instability of the devices.[91] This phenomenon is due to the adsorption of oxygen radicals on the deep electronic trap sites on the TiO_2 oxygen vacancies, which can react with photogenerated holes.[163,249] The oxygen is then released and leaves an electron trap state behind. The electrons which are trapped in these states will further recombine with holes.[249] A tri-block fullerene derivative layer, [6,6]-phenyl-C_{61}butyric acid-dioctyl-3,3′-(5-hydroxy-1,3-phenylene)-bis(2cyano-acrylate)ester (PCBB-2CN-2C8), was used to modify the temperature-processed TiO_2 surface in planar PSCs.[23] This interface engineering led to an enhanced charge extraction from the LHP layer to the TiO_2 layer as well as to the passivation of the TiO_2 surface. This resulted in an improved device performance (20.7% improvement) and enhanced stability of the PSCs. The TiO_2 surface traps were passivated by the tri-block fullerene, which resulted in an increase in stability of more than 4 times (from ~40 h to ~200 h shelf lifetime under ambient conditions). The stability of the PSCs was also enhanced by using a

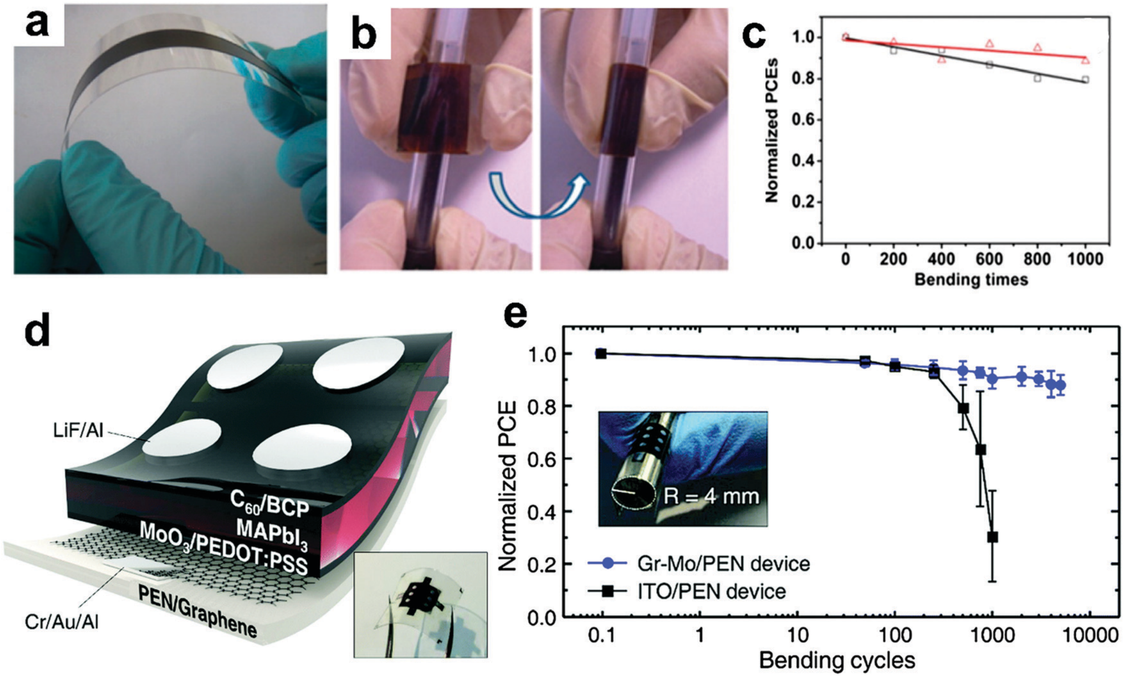

Fig. 12 Mechanical stability of carbon electrodes. (a) Conductive carbon films prepared on a plastic substrate, reprinted with permission.[148] (b) Photograph demonstrating the bending of the flexible ZnO/$CH_3NH_3PbI_3$/C PSCs around a pen with a diameter of 1 cm. (c) Normalized PCE variations during 1000 bending cycles for two randomly selected flexible devices, reprinted with permission.[216] (d) The device structure of GR-based flexible PSCs (inset image: photograph of a complete device). (e) Normalized PCEs as a function of bending cycles at a fixed bending radius of 4 mm for the GR-Mo/PEN and ITO/PEN devices. Average values from four separate devices are presented with error bars of standard deviation. The inset photograph shows the Gr-Mo/PEN device bent at a bending radius (*R*) of 4 mm, reprinted with permission.[104]

layer of lithium-neutralized GO (GO-Li) on top of the mesoporous TiO_2 layer, which was claimed to passivate the oxygen vacancies/defects on the mesoporous TiO_2 layer.[91]

An enhancement in the stability of the triple cation-based $MA_{0.57}FA_{0.38}Rb_{0.05}PbI_3$ PSCs was achieved by Mahmud *et al.*[250] applying carbon materials, fullerene (C_{60}) and $PC_{71}BM$ ([6,6]-phenyl C_{71} butyric acid methyl ester), at the interface between the LHP and ZnO ESL. The adsorbed fullerene (C-ZnO) and PCBM (P-ZnO) at the interface between the ESL and the LHP layer passivate the interstitial trap sites on the surface of the ESL. This passivation of the interstitial trap states upshifted the Fermi-level of the ESL and led to an increase in n-type conductivity. Devices with the C_{60} interlayer on the ESL showed high stability maintaining 94% of the initial PCE after one month, and the P-ZnO PSC retained nearly 88% of the PCE over the same time, while the ZnO reference device showed 81% of the initial PCE over one month. The stability test was carried out by storing the devices in an N_2-filled glovebox (in the dark) and measuring the device performance frequently under ambient conditions with controlled humidity (RH: 35–40%). The enhanced stability of devices based on the C-ZnO was mostly due to more stable J_{SC} and V_{OC} values in comparison to ZnO and P-ZnO PSCs. Mott–Schottky characterization was used to investigate trap-assisted charge recombination. The results showed that the flat band potential reduction for aged C-ZnO and P-ZnO PSCs was 10 mV, while this was 100 mV for the ZnO PSC, which indicates more significant trap-assisted recombination and thus lower normalized V_{OC} in the aged ZnO PSCs. The reason for the lower decrease in the normalized J_{SC} values of the C-ZnO devices is due to the higher hydrophobicity and lower charge trapping after the stability test.

Recently, Wang *et al.*[156] used chlorinated GO at the interface between LHP layer and HSL. The strong Pb–Cl and Pb–O bonds formed between lead in the LHP layer and chlorine and oxygen atoms in chlorinated GO layer constructed a heterostructure which can selectively extract photogenerated charge carriers and inhibit the loss of decomposed components from LHP layer to the HSL. Therefore, it reduced damage to the organic charge-transporting semiconductors. The PSCs maintained 90% of their initial PCE (21%) after the operation at the MPP under solar light at 60 °C for 1000 hours.

GR derivatives have been used between HSL and metal contact as an efficient barrier for ion migration and metal diffusion in PSCs. An enhancement in the stability of PSC was achieved by applying a spin-coated RGO passivation layer between HSL (CuSCN) and Au layer.[114] The device maintained more than 95% of its initial PCE after aging for 1000 hours under full-sun illumination at 60 °C. The RGO spacer layer suppressed unfavorable reaction between I^- ion and Au electrode. However, it is challenging to achieve a highly conductive and atomically thin RGO passivation layer by the spin coating process.

Lee *et al.*[246] used an atomically-thin impermeable conductive GR (3 layers) as the spacer layer between Au contact and HSL. The GR layer functioned as a conductive diffusion barrier between CuSCN layer and Au electrode blocking I^- ion migration and Au diffusion, in addition to act as a barrier for moisture intrusion. The PSC with GR interfacial layer retained >94% of its initial PCE after 30 days at 50% humidity.

In addition to the enhancement in carrier dynamics and energy level alignment designing, the interface with carbon materials also can serve as barriers against moisture permission and ion diffusion or migration. It can enhance device stability and provide a feasible solution to the stability challenge of PSCs.

3.6 Carbon with different functions in the same perovskite solar cell

The versatility of the carbon-based materials and their unique features provides the possibility of applying them in different parts of the PSCs simultaneously in order to improve the stability.[54,78] GO-based components have been applied as both HSLs and ESLs by Nouri *et al.* applying NiO–GO as HSL and GO–TiO_2 as the ESL in inverted PSCs (FTO/NiO/GO/LHP/GO-Li/TiO_x/Al). Although the device with the GO-based charge transport layers had lower PCE compared to the device with common components (FTO/PEDOT:PSS/LHP/PCBM/Al), it showed a better stability with negligible hysteresis.[191]

A metal contact-free carbon sandwich structure with a lead halide LHP layer between two allotropes of carbon (a fullerene layer as the bottom layer and SWCNTs as the top electrode) was developed by Ahn *et al.*[251] The graphical illustration of the device structure is shown in Fig. 13a. Due to the prevention of both moisture ingress and trapping of charges by fullerene and the hydrophobic SWCNTs, devices with the structure of ITO/C_{60}/$CH_3NH_3PbI_3$/CNT showed higher long-term stability in comparison to devices based on TiO_2 electrodes (under one sun illumination, without UV-filter and at ambient conditions), Fig. 13b. Even higher stabilities were obtained by using a combination of polymeric HSLs with CNTs, because of the strong interaction with CNTs and a more compact structure. Encapsulated devices stored at open-circuit condition under constant illumination of one sun illumination in ambient air maintained 80% of their efficiencies over 2200 h.[251]

An all-carbon electrode-based flexible PSC was fabricated by Luo *et al.*[252] by integrating GR and CNTs simultaneously into the PSC. CNTs were used for the cathode, and GR was applied as the anode to fabricate the flexible PSC. Fig. 13c displays the schematic of the configuration of the all-carbon electrode-based flexible device. The prepared flexible PSCs showed better mechanical durability against deformation compared to the devices made from flexible ITO substrates. The all-carbon electrode-based devices were able to retain about 84% of their initial efficiency after 2000 bending cycles using a bending curvature of 4 mm, while the PCE of the ITO-based flexible PSC decreased to 13% of its initial value after 1500 bending cycles, Fig. 13d. This is because of the dramatic increase in ohmic resistance of the ITO/PEN material after the bending cycles. However, the resistance of the CNT and GR electrode remained unchanged. Interestingly, the all-carbon-electrode also demonstrated superior stability compared to devices with Au or Ag cathodes under light or under thermal stress at 60 °C. The stability tests under light soaking conditions showed that the all-carbon electrode devices maintained 92% of their initial PCE after 1014 h, while the devices with Au and Ag electrodes retained 75% and 61% of their efficiencies, respectively. The devices were further subjected to constant temperature stress (60 °C, in dark) in air, Fig. 13e. The efficiencies of PSCs with Ag and Au electrodes decreased to 26% and 52% of their initial

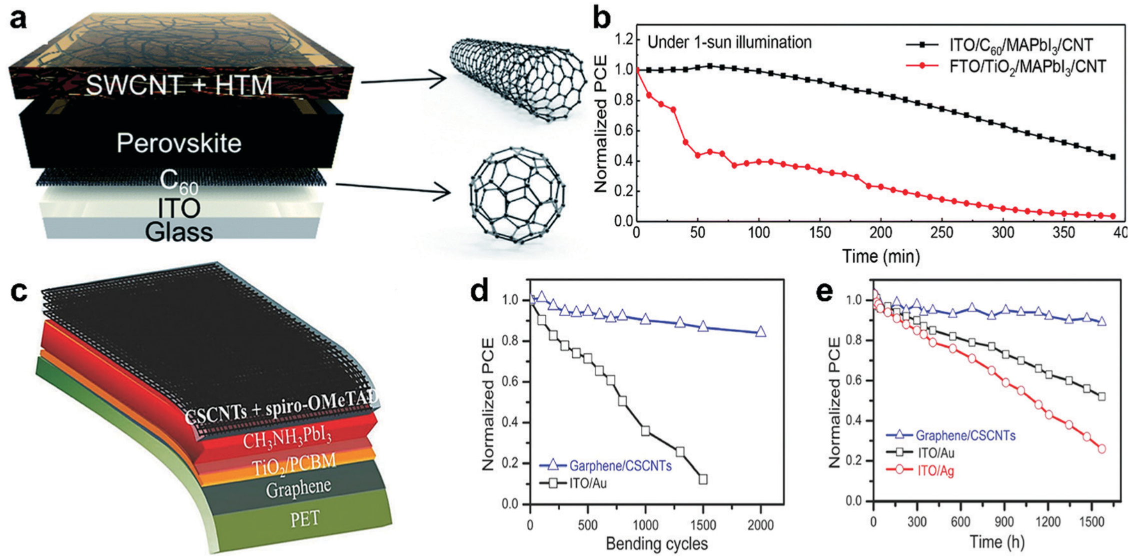

Fig. 13 Employing different carbon materials in various parts of PSCs simultaneously. (a) Schematic of the devices with LHP active layer sandwiched by fullerenes and CNTs entangled with a hole-transporting material. (b) Time evolution of normalized PCEs of C_{60}- and TiO_2-based devices without encapsulation, reprinted with permission.[251] (c) Schematic of the architecture of the all-carbon electrode-based flexible PSCs. CSCNTs stands for cross-stacked CNTs. (d) Bending durability of the ITO/PEN-based and all-carbon-electrode-based flexible solar cells as a function of bending cycles. (e) Stability of the standard and all-carbon electrode-based flexible PSCs as a function of soaking time in the ambient atmosphere under constant temperature stress (60 °C), reprinted with permission.[252]

values, which was ascribed to metal ion migration into the LHP absorber film as well as to accelerated moisture entry at higher temperatures, whereas the all-carbon electrode flexible PSCs retained 89% of the initial PCE after 1570 h.

4. Limitations

Application of carbon-based materials is a promising approach to improve the charge transfer, reduce charge recombination, enhance stability, and reduce the manufacturing cost of the PSCs. Nevertheless, there is still plenty room for further device performance and stability improvement. On the other hand, it requires a standardized test benchmark to make a legitimate comparison between PSCs based on different carbon materials.[155]

It is still challenging to control the diameter, crystallinity, and alignment of carbon-based materials simultaneously. The stability of carbon-based materials also needs to be enhanced. Moreover, the intrinsic properties of some of the carbon materials, such as conductivity and structure (amorphous or ordered), may cause issues in their functions in PSCs.

Fullerenes have been broadly used in PSCs. However, they suffer from some drawbacks, such as high cost and poor ambient stability, and low energy level variability because structurally they cannot easily undergo chemical modifications. Moreover, they tend to aggregate upon annealing which may result in poor film morphology.[253] Accordingly, the need to explore new ESLs was an incentive to develop an alternative that can overcome these deficiencies.

In the last few years, considerable efforts have been dedicated to the development of non-fullerene acceptors with acceptor–donor–acceptor structures. Non-fullerene acceptors such as ITIC (3,9-bis(2-methylene-((3-(1,1-dicyanomethylene)-6/7-methyl)-indanone))-5,5,11,11-tetrakis(4-hexylphenyl)-dithieno[2,3-*d*:2′,3′-*d*′]-*s*-indaceno[1,2-*b*:5,6*b*′]dithiophene), have tunable band gap. ITIC and its derivatives have demonstrated record power conversion efficiencies (PCEs) of over 10% to date.[253,254]

Another extensively used carbon-based material in PSCs is GR. CVD-grown GR can be an ideal electrode because of its high transparency and inertness. However, its application is limited due to the process issues. Although the structure–property relationships of other GR derivatives are routinely explored, there is no well-controlled and optimized fabrication process. It is because of the non-stoichiometric nature of GR and its derivatives with unclear empirical formulae.[255]

C-PSCs using the carbon electrode with high water resistance and thermal stability are one of the best choices for air-stable PSCs. On the contrary, their PCE is far behind the PCE of state-of-the-art PSCs with an organic or inorganic HSL and a metal electrode.[256] The commonly used carbon electrodes in C-PSCs (graphite and carbon black) do not have sufficient hole selectivity due to the slight mismatch in Fermi level with valence band of the LHP resulting in severe recombination loss. The other cause of their current low performance is poor contact at the interface between carbon and LHP and limitation in fabrication techniques.[238] This results in undesired charge recombination and low PCE.

The interface between carbon and LHP needs in-depth investigations. The poor contact between LHP and carbon electrode, which contains graphite flakes, encumber the hole extraction from the LHP to the carbon. For further improvements, the interfacial contact issues need to be overcome by interfacial engineering to take a positive step toward commercialization.[238] One of the most crucial concerns in the use of carbon-based materials for PSCs with high efficiency and long-term stability is that the process fundamentals are not clear enough for the industrial manufacturing approach.

On the other hand, some stability issues cannot be resolved by applying carbon-based materials. Internal factors such as ion migration, intrinsic molecular dissociation, interfacial reactions, and thermal instability of most LHPs are intrinsic sources of degradation of PSCs which have not been prevented efficiently by carbon-based materials.[243,257] Ion migration, which is an intrinsic and known issue in LHPs, is considered as one of the key challenges for improving the lifetime of PSCs. Ion migration is almost unavoidable in all types of LHPs due to their high ionic mobility. The situation is even more serious at defective sites, grain boundaries, and interfaces.[258] The mobile ions degrade the LHP and react with electron and hole and cause problems.

The intrinsic tendency for molecular dissociation of the LHPs to their starting precursor materials is also of great concern for the long-term stability of perovskite photovoltaics, and this cannot be hindered by the use of carbon-based materials. For instance, $MAPbX_3$ (X = I, Br, Cl) tends to decompose to MAX and PbX_2. A critical issue not yet properly addressed is the thermal instability of the LHP itself due to chemical and structural instabilities. It is well known that some LHPs undergo phase transitions and structural transformations in the temperature range relevant to photovoltaic applications in full sunlight (at or above about 85 °C).[155,259]

In general, LHP materials structurally belong to the class of soft materials and, consequently, should have a large response function to small external perturbations such as temperature increases.[260]

5. Summary and future directions

PSCs have progressed remarkably fast in just a few years and they are now approaching the performance of silicon-based photovoltaics. However, the long-term stability of PSC remains one of the most critical challenges to overcome. The upscaling and commercialization of this photovoltaic technology require the use of new materials that are inexpensive and enhance the stability of the device. Carbon-based materials have a variety of properties that make them ideal for photovoltaic applications. They are stable, inexpensive, and have been applied in all functional layers of the PSCs showing great potential in increasing the stability of the devices. Carbon materials are mostly water-resistant and impede the water ingress into the LHP layer resulting in higher stability under humid conditions. Thus, we expect to see many reports on incorporating carbon-based materials in PSCs, particularly for enhancing the stability, in this fast-evolving field.

For the application of LHPs in multi-junction solar cells or tandem devices, a transparent electrode on top of the LHP is needed. Developing relatively transparent carbon top electrodes such as GR and CNT networks will be essential for this application. One of the most promising PSC based on carbon is the C-PSC. The high stability has been shown to be a significant advantage of this type of PSCs. Nevertheless, the efficiencies of C-PSCs still need to be improved to make them competitive to state-of-the-art PSCs and silicon-based solar cells.

The stability of PSCs based on carbon materials requires more systematic studies under different operational conditions such as humidity, high temperature, light, or combinations of these. On the other hand, there are no universal "standard" protocols to compare the stability of devices. This makes it challenging to compare devices between groups. Thus, we need to establish a standardized protocol to evaluate the long-term stability of PSCs.

Furthermore, before bringing PSCs based on carbon materials to commercialization and launching them into the global market, parameters such as cost, environmental impact, and high stability need to be addressed.[261] The typical architectures and deposition techniques used in laboratories cannot be easily implemented to commercial solar cells.[261,262] and large-scale fabrication methods need to be developed to produce and commercialize long-term stable PSCs based on carbon materials.

Among the family of PSCs, C-PSCs (HSL-free PSCs with carbon counter electrode), in which the use of the expensive and unstable spiro-MeOTAD and gold are avoided, have great potential for commercialization of this new technology due to scalable deposition processes.[18,226,263] Large-area modules using carbon as cathode have been reported, exhibiting low cost, high throughput, and superior long-term stability.[226,264,265] Hu *et al.*[265] fabricated a hole-conductor-free printable solar module employing a triple layer of mesoporous TiO_2/ZrO_2/carbon as scaffold and $(5\text{-AVA})_x(MA)_{1-x}PbI_3$ LHP as the light harvester. The 10 × 10 cm^2 module with an active area of 49 cm^2 (PCE of 10.4%) showed over one-year shelf life in the dark under ambient conditions. It was also stable under light soaking test for 1000 h, or under outdoor test in the local environment for a month. Moreover, to assess the reproducibility, a 7 m^2 fully printable perovskite solar panel was fabricated in which each of the 1 m^2 panels was assembled using 96 solar modules. However, for better performance, apart from other parts of the module, the carbon counter electrode with smaller resistance needs to be developed.

The reports and progress on large-area modules show the potential of PSCs based on carbon materials for scaling up and commercialization. Nevertheless, to be able to convince the market to shift over for more advanced technologies, further research and developments are required.

Conflicts of interest

There are no conflicts of interest to declare.

Acknowledgements

M. H. and J. H. S. would like to acknowledge financial support from the Academy of Finland (grant no. 308307) and Jane and Aatos Erkko Foundation.

References

1 A. Polman, M. Knight, E. C. Garnett, B. Ehrler and W. C. Sinke, *Science*, 2016, **352**, aad4424.
2 J.-P. Correa-Baena, M. Saliba, T. Buonassisi, M. Grätzel, A. Abate, W. Tress and A. Hagfeldt, *Science*, 2017, **358**, 739–744.
3 M. Saliba, J.-P. Correa-Baena, C. M. Wolff, M. Stolterfoht, N. Phung, S. Albrecht, D. Neher and A. Abate, *Chem. Mater.*, 2018, **30**, 4193–4201.
4 W. E. I. Sha, X. Ren, L. Chen and W. C. H. Choy, *Appl. Phys. Lett.*, 2015, **106**, 221104.
5 S. Mahesh, J. M. Ball, R. D. J. Oliver, D. P. McMeekin, P. K. Nayak, M. B. Johnston and H. J. Snaith, *Energy Environ. Sci.*, 2020, **13**, 258–267.
6 NREL, Efficiency chart, https://www.nrel.gov/pv/assets/pdfs/best-research-cell-efficiencies.20190923.pdf, 2019.
7 S. Sun, T. Buonassisi and J.-P. Correa-Baena, *Adv. Mater. Interfaces*, 2018, **5**, 1800408.
8 H. Wei and J. Huang, *Nat. Commun.*, 2019, **10**, 1066.
9 P. Gao, M. Grätzel and M. K. Nazeeruddin, *Energy Environ. Sci.*, 2014, **7**, 2448–2463.
10 Y. Yang and J. You, *Nature*, 2017, **544**, 155.
11 M. Saliba, *Science*, 2018, **359**, 388–389.
12 S.-W. Lee, S. Kim, S. Bae, K. Cho, T. Chung, L. E. Mundt, S. Lee, S. Park, H. Park, M. C. Schubert, S. W. Glunz, Y. Ko, Y. Jun, Y. Kang, H.-S. Lee and D. Kim, *Sci. Rep.*, 2016, **6**, 38150.
13 M. V. Khenkin, K. M. Anoop, E. A. Katz and I. Visoly-Fisher, *Energy Environ. Sci.*, 2019, **12**, 550–558.
14 M. Saliba, T. Matsui, J.-Y. Seo, K. Domanski, J.-P. Correa-Baena, M. K. Nazeeruddin, S. M. Zakeeruddin, W. Tress, A. Abate, A. Hagfeldt and M. Grätzel, *Energy Environ. Sci.*, 2016, **9**, 1989–1997.
15 S. N. Habisreutinger, D. P. McMeekin, H. J. Snaith and R. J. Nicholas, *APL Mater.*, 2016, **4**, 091503.
16 H. Tsai, W. Nie, J.-C. Blancon, C. C. Stoumpos, R. Asadpour, B. Harutyunyan, A. J. Neukirch, R. Verduzco, J. J. Crochet, S. Tretiak, L. Pedesseau, J. Even, M. A. Alam, G. Gupta, J. Lou, P. M. Ajayan, M. J. Bedzyk, M. G. Kanatzidis and A. D. Mohite, *Nature*, 2016, **536**, 312.
17 H. Chen and S. Yang, *J. Mater. Res.*, 2017, **32**, 3011–3020.
18 Y. Cai, L. Liang and P. Gao, *Chin. Phys. B*, 2018, **27**, 018805.
19 Z. Wu, T. Song and B. Sun, *ChemNanoMat*, 2017, **3**, 75–88.
20 L. Fagiolari and F. Bella, *Energy Environ. Sci.*, 2019, **12**, 3437–3472.
21 L. K. Shrestha, Q. Ji, T. Mori, K. i. Miyazawa, Y. Yamauchi, J. P. Hill and K. Ariga, *Chem. – Asian J.*, 2013, **8**, 1662–1679.
22 S. D. Stranks, G. E. Eperon, G. Grancini, C. Menelaou, M. J. P. Alcocer, T. Leijtens, L. M. Herz, A. Petrozza and H. J. Snaith, *Science*, 2013, **342**, 341–344.

23 Y. Li, Y. Zhao, Q. Chen, Y. Yang, Y. Liu, Z. Hong, Z. Liu, Y.-T. Hsieh, L. Meng, Y. Li and Y. Yang, *J. Am. Chem. Soc.*, 2015, **137**, 15540–15547.

24 A. Abrusci, S. D. Stranks, P. Docampo, H.-L. Yip, A. K. Y. Jen and H. J. Snaith, *Nano Lett.*, 2013, **13**, 3124–3128.

25 G. Xu, R. Xue, W. Chen, J. Zhang, M. Zhang, H. Chen, C. Cui, H. Li, Y. Li and Y. Li, *Adv. Energy Mater.*, 2018, **8**, 1703054.

26 Y. Fang, C. Bi, D. Wang and J. Huang, *ACS Energy Lett.*, 2017, **2**, 782–794.

27 J. Xu, A. Buin, A. H. Ip, W. Li, O. Voznyy, R. Comin, M. Yuan, S. Jeon, Z. Ning, J. J. McDowell, P. Kanjanaboos, J.-P. Sun, X. Lan, L. N. Quan, D. H. Kim, I. G. Hill, P. Maksymovych and E. H. Sargent, *Nat. Commun.*, 2015, **6**, 7081.

28 Y. Shao, Z. Xiao, C. Bi, Y. Yuan and J. Huang, *Nat. Commun.*, 2014, **5**, 5784.

29 F. Xia, Q. Wu, P. Zhou, Y. Li, X. Chen, Q. Liu, J. Zhu, S. Dai, Y. Lu and S. Yang, *ACS Appl. Mater. Interfaces*, 2015, **7**, 13659–13665.

30 K. Zhu, T. Miyasaka, J. Y. Kim and I. Mora-Seró, *J. Phys. Chem. Lett.*, 2015, **6**, 2315–2317.

31 Z. Chu, M. Yang, P. Schulz, D. Wu, X. Ma, E. Seifert, L. Sun, X. Li, K. Zhu and K. Lai, *Nat. Commun.*, 2017, **8**, 2230.

32 J. Pascual, S. Collavini, S. F. Völker, N. Phung, E. Palacios-Lidon, L. Irusta, H.-J. Grande, A. Abate, R. Tena-Zaera and J. L. Delgado, *Sustainable Energy Fuels*, 2019, **3**, 2779–2787.

33 Q. Fu, S. Xiao, X. Tang, Y. Chen and T. Hu, *ACS Appl. Mater. Interfaces*, 2019, **11**, 24782–24788.

34 E. Castro, J. Murillo, O. Fernandez-Delgado and L. Echegoyen, *J. Mater. Chem. C*, 2018, **6**, 2635–2651.

35 J.-Y. Jeng, Y.-F. Chiang, M.-H. Lee, S.-R. Peng, T.-F. Guo, P. Chen and T.-C. Wen, *Adv. Mater.*, 2013, **25**, 3727–3732.

36 S. F. Völker, S. Collavini and J. L. Delgado, *ChemSusChem*, 2015, **8**, 3012–3028.

37 L. Meng, J. You, T.-F. Guo and Y. Yang, *Acc. Chem. Res.*, 2016, **49**, 155–165.

38 P. Docampo, J. M. Ball, M. Darwich, G. E. Eperon and H. J. Snaith, *Nat. Commun.*, 2013, **4**, 2761.

39 O. Malinkiewicz, A. Yella, Y. H. Lee, G. M. Espallargas, M. Graetzel, M. K. Nazeeruddin and H. J. Bolink, *Nat. Photonics*, 2013, **8**, 128.

40 J. Seo, S. Park, Y. Chan Kim, N. J. Jeon, J. H. Noh, S. C. Yoon and S. I. Seok, *Energy Environ. Sci.*, 2014, **7**, 2642–2646.

41 C.-H. Chiang, Z.-L. Tseng and C.-G. Wu, *J. Mater. Chem. A*, 2014, **2**, 15897–15903.

42 W. Nie, H. Tsai, R. Asadpour, J.-C. Blancon, A. J. Neukirch, G. Gupta, J. J. Crochet, M. Chhowalla, S. Tretiak, M. A. Alam, H.-L. Wang and A. D. Mohite, *Science*, 2015, **347**, 522–525.

43 S.-M. Dai, X. Zhang, W.-Y. Chen, X. Li, Z. A. Tan, C. Li, L.-L. Deng, X.-X. Zhan, M.-S. Lin, Z. Xing, T. Wen, R.-M. Ho, S.-Y. Xie, R.-B. Huang and L.-S. Zheng, *J. Mater. Chem. A*, 2016, **4**, 18776–18782.

44 Y. Shao, Y. Yuan and J. Huang, *Nat. Energy*, 2016, **1**, 15001.

45 C.-H. Chiang, M. K. Nazeeruddin, M. Grätzel and C.-G. Wu, *Energy Environ. Sci.*, 2017, **10**, 808–817.

46 X. Zheng, B. Chen, J. Dai, Y. Fang, Y. Bai, Y. Lin, H. Wei, X. C. Zeng and J. Huang, *Nat. Energy*, 2017, **2**, 17102.

47 M. Li, Z.-K. Wang, T. Kang, Y. Yang, X. Gao, C.-S. Hsu, Y. Li and L.-S. Liao, *Nano Energy*, 2018, **43**, 47–54.

48 D. Luo, W. Yang, Z. Wang, A. Sadhanala, Q. Hu, R. Su, R. Shivanna, G. F. Trindade, J. F. Watts, Z. Xu, T. Liu, K. Chen, F. Ye, P. Wu, L. Zhao, J. Wu, Y. Tu, Y. Zhang, X. Yang, W. Zhang, R. H. Friend, Q. Gong, H. J. Snaith and R. Zhu, *Science*, 2018, **360**, 1442–1446.

49 X. Liu, Y. Cheng, C. Liu, T. Zhang, N. Zhang, S. Zhang, J. Chen, Q. Xu, J. Ouyang and H. Gong, *Energy Environ. Sci.*, 2019, **12**, 1622–1633.

50 S. Vidal, M. Izquierdo, S. Filippone, I. Fernández, S. Akin, J.-Y. Seo, S. M. Zakeeruddin, M. Grätzel and N. Martín, *Chem. – Eur. J.*, 2019, **25**, 3224–3228.

51 D. Yang, X. Zhang, K. Wang, C. Wu, R. Yang, Y. Hou, Y. Jiang, S. Liu and S. Priya, *Nano Lett.*, 2019, **19**, 3313–3320.

52 P.-W. Liang, C.-Y. Liao, C.-C. Chueh, F. Zuo, S. T. Williams, X.-K. Xin, J. Lin and A. K.-Y. Jen, *Adv. Mater.*, 2014, **26**, 3748–3754.

53 E. Castro, G. Zavala, S. Seetharaman, F. D'Souza and L. Echegoyen, *J. Mater. Chem. A*, 2017, **5**, 19485–19490.

54 X. Meng, J. Zhou, J. Hou, X. Tao, S. H. Cheung, S. K. So and S. Yang, *Adv. Mater.*, 2018, **30**, 1706975.

55 T. Umeyama, D. Matano, S. Shibata, J. Baek, S. Ito and H. Imahori, *ECS J. Solid State Sci. Technol.*, 2017, **6**, M3078–M3083.

56 Q.-Q. Ye, Z.-K. Wang, M. Li, C.-C. Zhang, K.-H. Hu and L.-S. Liao, *ACS Energy Lett.*, 2018, **3**, 875–882.

57 X. Gao, Y. Zhu, D. Yi, J. Zhou, S. Zhang, C. Yin, F. Ding, S. Zhang, X. Yi, J. Wang, L. Tong, Y. Han, Z. Liu and J. Zhang, *Sci. Adv.*, 2018, **4**, eaat6378.

58 K. Wang, C. Liu, P. Du, J. Zheng and X. Gong, *Energy Environ. Sci.*, 2015, **8**, 1245–1255.

59 R. Sandoval-Torrientes, J. Pascual, I. García-Benito, S. Collavini, I. Kosta, R. Tena-Zaera, N. Martín and J. L. Delgado, *ChemSusChem*, 2017, **10**, 2023–2029.

60 C. Liu, K. Wang, P. Du, C. Yi, T. Meng and X. Gong, *Adv. Energy Mater.*, 2015, **5**, 1402024.

61 Y. Wu, X. Yang, W. Chen, Y. Yue, M. Cai, F. Xie, E. Bi, A. Islam and L. Han, *Nat. Energy*, 2016, **1**, 16148.

62 Y. Zhao, W. Zhou, W. Ma, S. Meng, H. Li, J. Wei, R. Fu, K. Liu, D. Yu and Q. Zhao, *ACS Energy Lett.*, 2016, **1**, 266–272.

63 B. Chen, M. Yang, S. Priya and K. Zhu, *J. Phys. Chem. Lett.*, 2016, **7**, 905–917.

64 K. Wojciechowski, S. D. Stranks, A. Abate, G. Sadoughi, A. Sadhanala, N. Kopidakis, G. Rumbles, C.-Z. Li, R. H. Friend, A. K. Y. Jen and H. J. Snaith, *ACS Nano*, 2014, **8**, 12701–12709.

65 S. N. Habisreutinger, T. Leijtens, G. E. Eperon, S. D. Stranks, R. J. Nicholas and H. J. Snaith, *Nano Lett.*, 2014, **14**, 5561–5568.

66 K. Aitola, K. Sveinbjörnsson, J.-P. Correa-Baena, A. Kaskela, A. Abate, Y. Tian, E. M. J. Johansson, M. Grätzel, E. I. Kauppinen, A. Hagfeldt and G. Boschloo, *Energy Environ. Sci.*, 2016, **9**, 461–466.

67 A. Monreal-Bernal, M. Bidikoudi and R. D. Costa, in *Carbon Based Nanomaterials for Advanced Thermal and Electrochemical Energy Storage and Conversion*, ed. R. Paul, V. Etacheri, Y. Wang and C.-T. Lin, Elsevier, 2019.

68 Y. Zhang, L. Tan, Q. Fu, L. Chen, T. Ji, X. Hu and Y. Chen, *Chem. Commun.*, 2016, **52**, 5674–5677.

69 S. Seo, I. Jeon, R. Xiang, C. Lee, H. Zhang, T. Tanaka, J.-W. Lee, D. Suh, T. Ogamoto, R. Nishikubo, A. Saeki, S. Chiashi, J. Shiomi, H. Kataura, H. M. Lee, Y. Yang, Y. Matsuo and S. Maruyama, *J. Mater. Chem. A*, 2019, **7**, 12987–12992.

70 Z. Li, S. A. Kulkarni, P. P. Boix, E. Shi, A. Cao, K. Fu, S. K. Batabyal, J. Zhang, Q. Xiong, L. H. Wong, N. Mathews and S. G. Mhaisalkar, *ACS Nano*, 2014, **8**, 6797–6804.

71 L. Qiu, J. Deng, X. Lu, Z. Yang and H. Peng, *Angew. Chem., Int. Ed.*, 2014, **53**, 10425–10428.

72 S. N. Habisreutinger, T. Leijtens, G. E. Eperon, S. D. Stranks, R. J. Nicholas and H. J. Snaith, *J. Phys. Chem. Lett.*, 2014, **5**, 4207–4212.

73 S. N. Habisreutinger, R. J. Nicholas and H. J. Snaith, *Adv. Energy Mater.*, 2017, **7**, 1601839.

74 L. Qiu, S. He, J. Yang, J. Deng and H. Peng, *Small*, 2016, **12**, 2419–2424.

75 A. Balilonda, Q. Li, M. Tebyetekerwa, R. Tusiime, H. Zhang, R. Jose, F. Zabihi, S. Yang, S. Ramakrishna and M. Zhu, *Adv. Fiber Mater.*, 2019, **1**, 101–125.

76 J. Geng and T. Zeng, *J. Am. Chem. Soc.*, 2006, **128**, 16827–16833.

77 A. Phuong, Le, T.-M. Huang, P.-T. Chen and A. C.-M. Yang, *J. Polym. Sci., Part B: Polym. Phys.*, 2011, **49**, 581–590.

78 I. Jeon, S. Seo, Y. Sato, C. Delacou, A. Anisimov, K. Suenaga, E. I. Kauppinen, S. Maruyama and Y. Matsuo, *J. Phys. Chem. C*, 2017, **121**, 25743–25749.

79 F. Bonaccorso, Z. Sun, T. Hasan and A. C. Ferrari, *Nat. Photonics*, 2010, **4**, 611–622.

80 E. L. Lim, C. C. Yap, M. H. H. Jumali, M. A. M. Teridi and C. H. Teh, *Nano-Micro Lett.*, 2017, **10**, 27.

81 S. Das, D. Pandey, J. Thomas and T. Roy, *Adv. Mater.*, 2019, **31**, 1802722.

82 P. You, Z. Liu, Q. Tai, S. Liu and F. Yan, *Adv. Mater.*, 2015, **27**, 3632–3638.

83 Z. Liu, P. You, C. Xie, G. Tang and F. Yan, *Nano Energy*, 2016, **28**, 151–157.

84 H. Sung, N. Ahn, M. S. Jang, J.-K. Lee, H. Yoon, N.-G. Park and M. Choi, *Adv. Energy Mater.*, 2016, **6**, 1501873.

85 X. Fang, J. Ding, N. Yuan, P. Sun, M. Lv, G. Ding and C. Zhu, *Phys. Chem. Chem. Phys.*, 2017, **19**, 6057–6063.

86 M. Hadadian, J.-P. Correa-Baena, E. K. Goharshadi, A. Ummadisingu, J.-Y. Seo, J. Luo, S. Gholipour, S. M. Zakeeruddin, M. Saliba, A. Abate, M. Grätzel and A. Hagfeldt, *Adv. Mater.*, 2016, **28**, 8681–8686.

87 J.-S. Yeo, C.-H. Lee, D. Jang, S. Lee, S. M. Jo, H.-I. Joh and D.-Y. Kim, *Nano Energy*, 2016, **30**, 667–676.

88 K. Yan, Z. Wei, J. Li, H. Chen, Y. Yi, X. Zheng, X. Long, Z. Wang, J. Wang, J. Xu and S. Yang, *Small*, 2015, **11**, 2269–2274.

89 G. Yang, H. Tao, P. Qin, W. Ke and G. Fang, *J. Mater. Chem. A*, 2016, **4**, 3970–3990.

90 J. T.-W. Wang, J. M. Ball, E. M. Barea, A. Abate, J. A. Alexander-Webber, J. Huang, M. Saliba, I. Mora-Sero, J. Bisquert, H. J. Snaith and R. J. Nicholas, *Nano Lett.*, 2014, **14**, 724–730.

91 A. Agresti, S. Pescetelli, L. Cinà, D. Konios, G. Kakavelakis, E. Kymakis and A. D. Carlo, *Adv. Funct. Mater.*, 2016, **26**, 2686–2694.

92 X. Zhang, G. Ji, D. Xiong, Z. Su, B. Zhao, K. Shen, Y. Yang and X. Gao, *RSC Adv.*, 2018, **8**, 987–993.

93 H.-S. Kim, C.-R. Lee, J.-H. Im, K.-B. Lee, T. Moehl, A. Marchioro, S.-J. Moon, R. Humphry-Baker, J.-H. Yum, J. E. Moser, M. Grätzel and N.-G. Park, *Sci. Rep.*, 2012, **2**, 591.

94 J. P. Correa Baena, L. Steier, W. Tress, M. Saliba, S. Neutzner, T. Matsui, F. Giordano, T. J. Jacobsson, A. R. Srimath Kandada, S. M. Zakeeruddin, A. Petrozza, A. Abate, M. K. Nazeeruddin, M. Grätzel and A. Hagfeldt, *Energy Environ. Sci.*, 2015, **8**, 2928–2934.

95 T. Liu, D. Kim, H. Han, A. R. b. Mohd Yusoff and J. Jang, *Nanoscale*, 2015, **7**, 10708–10718.

96 Z. Wu, S. Bai, J. Xiang, Z. Yuan, Y. Yang, W. Cui, X. Gao, Z. Liu, Y. Jin and B. Sun, *Nanoscale*, 2014, **6**, 10505–10510.

97 D. Li, J. Cui, H. Li, D. Huang, M. Wang and Y. Shen, *Sol. Energy*, 2016, **131**, 176–182.

98 Q.-D. Yang, J. Li, Y. Cheng, H.-W. Li, Z. Guan, B. Yu and S.-W. Tsang, *J. Mater. Chem. A*, 2017, **5**, 9852–9858.

99 J.-S. Yeo, R. Kang, S. Lee, Y.-J. Jeon, N. Myoung, C.-L. Lee, D.-Y. Kim, J.-M. Yun, Y.-H. Seo, S.-S. Kim and S.-I. Na, *Nano Energy*, 2015, **12**, 96–104.

100 C. Sun and D. J. Searles, *J. Phys. Chem. C*, 2012, **116**, 26222–26226.

101 Y. Xue, Y. Li, J. Zhang, Z. Liu and Y. Zhao, *Sci. China: Chem.*, 2018, **61**, 765–786.

102 J. Xiao, J. Shi, H. Liu, Y. Xu, S. Lv, Y. Luo, D. Li, Q. Meng and Y. Li, *Adv. Energy Mater.*, 2015, **5**, 1401943.

103 M. Batmunkh, C. J. Shearer, M. J. Biggs and J. G. Shapter, *J. Mater. Chem. A*, 2016, **4**, 2605–2616.

104 J. Yoon, H. Sung, G. Lee, W. Cho, N. Ahn, H. S. Jung and M. Choi, *Energy Environ. Sci.*, 2017, **10**, 337–345.

105 A. Agresti, S. Pescetelli, A. L. Palma, A. E. Del Rio Castillo, D. Konios, G. Kakavelakis, S. Razza, L. Cinà, E. Kymakis, F. Bonaccorso and A. Di Carlo, *ACS Energy Lett.*, 2017, **2**, 279–287.

106 G.-H. Kim, H. Jang, Y. J. Yoon, J. Jeong, S. Y. Park, B. Walker, I.-Y. Jeon, Y. Jo, H. Yoon, M. Kim, J.-B. Baek, D. S. Kim and J. Y. Kim, *Nano Lett.*, 2017, **17**, 6385–6390.

107 C. Wang, Y. Tang, Y. Hu, L. Huang, J. Fu, J. Jin, W. Shi, L. Wang and W. Yang, *RSC Adv.*, 2015, **5**, 52041–52047.

108 X. Zhao, L. Tao, H. Li, W. Huang, P. Sun, J. Liu, S. Liu, Q. Sun, Z. Cui, L. Sun, Y. Shen, Y. Yang and M. Wang, *Nano Lett.*, 2018, **18**, 2442–2449.

109 D. H. Shin, J. M. Kim, S. H. Shin and S.-H. Choi, *Dyes Pigm.*, 2019, **170**, 107630.

110 H. Bian, Q. Wang, S. Yang, C. Yan, H. Wang, L. Liang, Z. Jin, G. Wang and S. Liu, *J. Mater. Chem. A*, 2019, **7**, 5740–5747.

111 Y. Zhou, S. Yang, X. Yin, J. Han, M. Tai, X. Zhao, H. Chen, Y. Gu, N. Wang and H. Lin, *J. Mater. Chem. A*, 2019, **7**, 1878–1888.

112 M. M. Tavakoli, R. Tavakoli, P. Yadav and J. Kong, *J. Mater. Chem. A*, 2019, **7**, 679–686.

113 X. Meng, X. Cui, M. Rager, S. Zhang, Z. Wang, J. Yu, Y. W. Harn, Z. Kang, B. K. Wagner, Y. Liu, C. Yu, J. Qiu and Z. Lin, *Nano Energy*, 2018, **52**, 123–133.

114 N. Arora, M. I. Dar, A. Hinderhofer, N. Pellet, F. Schreiber, S. M. Zakeeruddin and M. Grätzel, *Science*, 2017, **358**, 768–771.

115 G. S. Han, Y. H. Song, Y. U. Jin, J.-W. Lee, N.-G. Park, B. K. Kang, J.-K. Lee, I. S. Cho, D. H. Yoon and H. S. Jung, *ACS Appl. Mater. Interfaces*, 2015, **7**, 23521–23526.

116 M. M. Tavakoli, R. Tavakoli, Z. Nourbakhsh, A. Waleed, U. S. Virk and Z. Fan, *Adv. Mater. Interfaces*, 2016, **3**, 1500790.

117 K. T. Cho, G. Grancini, Y. Lee, D. Konios, S. Paek, E. Kymakis and M. K. Nazeeruddin, *ChemSusChem*, 2016, **9**, 3040–3044.

118 N. Balis, A. A. Zaky, C. Athanasekou, A. M. T. Silva, E. Sakellis, M. Vasilopoulou, T. Stergiopoulos, A. G. Kontos and P. Falaras, *J. Photochem. Photobiol., A*, 2020, **386**, 112141.

119 T. Umeyama, D. Matano, J. Baek, S. Gupta, S. Ito, V. Subramanian and H. Imahori, *Chem. Lett.*, 2015, **44**, 1410–1412.

120 M. Li, W.-W. Zuo, Q. Wang, K.-L. Wang, M.-P. Zhuo, H. Köbler, C. E. Halbig, S. Eigler, Y.-G. Yang, X.-Y. Gao, Z.-K. Wang, Y. Li and A. Abate, *Adv. Energy Mater.*, 2020, **10**, 1902653.

121 H. Li, L. Tao, F. Huang, Q. Sun, X. Zhao, J. Han, Y. Shen and M. Wang, *ACS Appl. Mater. Interfaces*, 2017, **9**, 38967–38976.

122 Q. Luo, Y. Zhang, C. Liu, J. Li, N. Wang and H. Lin, *J. Mater. Chem. A*, 2015, **3**, 15996–16004.

123 E. Jokar, Z. Y. Huang, S. Narra, C.-Y. Wang, V. Kattoor, C.-C. Chung and E. W.-G. Diau, *Adv. Energy Mater.*, 2018, **8**, 1701640.

124 Y. Wang, Y. Hu, D. Han, Q. Yuan, T. Cao, N. Chen, D. Zhou, H. Cong and L. Feng, *Org. Electron.*, 2019, **70**, 63–70.

125 S. Ameen, M. S. Akhtar, M. Nazim, E.-B. Kim, M. K. Nazeeruddin and H.-S. Shin, *Electrochim. Acta*, 2019, **319**, 885–894.

126 Y. G. Kim, K. C. Kwon, Q. V. Le, K. Hong, H. W. Jang and S. Y. Kim, *J. Power Sources*, 2016, **319**, 1–8.

127 C.-C. Chung, S. Narra, E. Jokar, H.-P. Wu and E. Wei-Guang Diau, *J. Mater. Chem. A*, 2017, **5**, 13957–13965.

128 S. Feng, Y. Yang, M. Li, J. Wang, Z. Cheng, J. Li, G. Ji, G. Yin, F. Song, Z. Wang, J. Li and X. Gao, *ACS Appl. Mater. Interfaces*, 2016, **8**, 14503–14512.

129 Ç. Şahin, H. Diker, D. Sygkridou, C. Varlikli and E. Stathatos, *Renewable Energy*, 2020, **146**, 1659–1666.

130 L. Pietronero, S. Strässler, H. R. Zeller and M. J. Rice, *Phys. Rev. B: Condens. Matter Mater. Phys.*, 1980, **22**, 904–910.

131 F. Cataldo, *Fullerenes, Nanotubes, Carbon Nanostruct.*, 2002, **10**, 293–311.

132 H.-Q. Li, Y.-G. Wang, C.-X. Wang and Y.-Y. Xia, *J. Power Sources*, 2008, **185**, 1557–1562.

133 R. Hu, L. Chu, J. Zhang, X. a. Li and W. Huang, *J. Power Sources*, 2017, **361**, 259–275.

134 Z. Ku, Y. Rong, M. Xu, T. Liu and H. Han, *Sci. Rep.*, 2013, **3**, 3132.

135 A. Ciccioli and A. Latini, *J. Phys. Chem. Lett.*, 2018, **9**, 3756–3765.

136 M. Hu, L. Liu, A. Mei, Y. Yang, T. Liu and H. Han, *J. Mater. Chem. A*, 2014, **2**, 17115–17121.

137 Y. Rong, Z. Ku, A. Mei, T. Liu, M. Xu, S. Ko, X. Li and H. Han, *J. Phys. Chem. Lett.*, 2014, **5**, 2160–2164.

138 Y. Xiao, C. Wang, K. K. Kondamareddy, P. Liu, F. Qi, H. Zhang, S. Guo and X.-Z. Zhao, *J. Power Sources*, 2019, **422**, 138–144.

139 A. Mei, X. Li, L. Liu, Z. Ku, T. Liu, Y. Rong, M. Xu, M. Hu, J. Chen, Y. Yang, M. Grätzel and H. Han, *Science*, 2014, **345**, 295–298.

140 Y. Yang, K. Ri, A. Mei, L. Liu, M. Hu, T. Liu, X. Li and H. Han, *J. Mater. Chem. A*, 2015, **3**, 9103–9107.

141 Y. Sheng, Y. Hu, A. Mei, P. Jiang, X. Hou, M. Duan, L. Hong, Y. Guan, Y. Rong, Y. Xiong and H. Han, *J. Mater. Chem. A*, 2016, **4**, 16731–16736.

142 H. Zhang, H. Wang, S. T. Williams, D. Xiong, W. Zhang, C.-C. Chueh, W. Chen and A. K.-Y. Jen, *Adv. Mater.*, 2017, **29**, 1606608.

143 J. Liu, Q. Zhou, N. K. Thein, L. Tian, D. Jia, E. M. J. Johansson and X. Zhang, *J. Mater. Chem. A*, 2019, **7**, 13777–13786.

144 Z. Wei, K. Yan, H. Chen, Y. Yi, T. Zhang, X. Long, J. Li, L. Zhang, J. Wang and S. Yang, *Energy Environ. Sci.*, 2014, **7**, 3326–3333.

145 H. Chen, X. Zheng, Q. Li, Y. Yang, S. Xiao, C. Hu, Y. Bai, T. Zhang, K. S. Wong and S. Yang, *J. Mater. Chem. A*, 2016, **4**, 12897–12912.

146 H. Chen, Z. Wei, X. Zheng and S. Yang, *Nano Energy*, 2015, **15**, 216–226.

147 H. Chen and S. Yang, *Adv. Mater.*, 2017, **29**, 1603994.

148 H. Zhou, Y. Shi, Q. Dong, H. Zhang, Y. Xing, K. Wang, Y. Du and T. Ma, *J. Phys. Chem. Lett.*, 2014, **5**, 3241–3246.

149 Y. Sheng, A. Mei, S. Liu, M. Duan, P. Jiang, C. Tian, Y. Xiong, Y. Rong, H. Han and Y. Hu, *J. Mater. Chem. A*, 2018, **6**, 2360–2364.

150 F. Zhang, X. Yang, M. Cheng, J. Li, W. Wang, H. Wang and L. Sun, *J. Mater. Chem. A*, 2015, **3**, 24272–24280.

151 Y. Xiong, Y. Liu, K. Lan, A. Mei, Y. Sheng, D. Zhao and H. Han, *New J. Chem.*, 2018, **42**, 2669–2674.

152 M. Duan, C. Tian, Y. Hu, A. Mei, Y. Rong, Y. Xiong, M. Xu, Y. Sheng, P. Jiang, X. Hou, X. Zhu, F. Qin and H. Han, *ACS Appl. Mater. Interfaces*, 2017, **9**, 31721–31727.

153 Y. Rong, X. Hou, Y. Hu, A. Mei, L. Liu, P. Wang and H. Han, *Nat. Commun.*, 2017, **8**, 14555.

154 M. Alsari, A. J. Pearson, J. T.-W. Wang, Z. Wang, A. Montisci, N. C. Greenham, H. J. Snaith, S. Lilliu and R. H. Friend, *Sci. Rep.*, 2018, **8**, 5977.

155 M. V. Khenkin, E. A. Katz, A. Abate, G. Bardizza, J. J. Berry, C. Brabec, F. Brunetti, V. Bulović, Q. Burlingame, A. Di Carlo, R. Cheacharoen, Y.-B. Cheng, A. Colsmann, S. Cros,

K. Domanski, M. Dusza, C. J. Fell, S. R. Forrest, Y. Galagan, D. Di Girolamo, M. Grätzel, A. Hagfeldt, E. von Hauff, H. Hoppe, J. Kettle, H. Köbler, M. S. Leite, S. Liu, Y.-L. Loo, J. M. Luther, C.-Q. Ma, M. Madsen, M. Manceau, M. Matheron, M. McGehee, R. Meitzner, M. K. Nazeeruddin, A. F. Nogueira, Ç. Odabaşı, A. Osherov, N.-G. Park, M. O. Reese, F. De Rossi, M. Saliba, U. S. Schubert, H. J. Snaith, S. D. Stranks, W. Tress, P. A. Troshin, V. Turkovic, S. Veenstra, I. Visoly-Fisher, A. Walsh, T. Watson, H. Xie, R. Yıldırım, S. M. Zakeeruddin, K. Zhu and M. Lira-Cantu, *Nat. Energy*, 2020, **5**, 35–49.

156 Y. Wang, T. Wu, J. Barbaud, W. Kong, D. Cui, H. Chen, X. Yang and L. Han, *Science*, 2019, **365**, 687–691.

157 R. Wang, M. Mujahid, Y. Duan, Z.-K. Wang, J. Xue and Y. Yang, *Adv. Funct. Mater.*, 2019, **29**, 1808843.

158 Q.-M. Hong, R.-P. Xu, T.-Y. Jin, J.-X. Tang and Y.-Q. Li, *Org. Electron.*, 2019, **67**, 19–25.

159 S. Y. Luchkin, A. F. Akbulatov, L. A. Frolova, M. P. Griffin, A. Dolocan, R. Gearba, D. A. Vanden Bout, P. A. Troshin and K. J. Stevenson, *ACS Appl. Mater. Interfaces*, 2017, **9**, 33478–33483.

160 S. Bae, S. Kim, S.-W. Lee, K. J. Cho, S. Park, S. Lee, Y. Kang, H.-S. Lee and D. Kim, *J. Phys. Chem. Lett.*, 2016, **7**, 3091–3096.

161 M. Batmunkh, T. J. Macdonald, C. J. Shearer, M. Bat-Erdene, Y. Wang, M. J. Biggs, I. P. Parkin, T. Nann and J. G. Shapter, *Adv. Sci.*, 2017, **4**, 1600504.

162 X. Shao, W. Lu, R. Zhang and F. Pan, *Sci. Rep.*, 2013, **3**, 3018.

163 Y. Zhou, J. Hu, Y. Wu, R. Qing, C. Zhang, X. Xu and M. Jiang, *J. Photonics Energy*, 2019, **9**, 040901.

164 M. Batmunkh, C. J. Shearer, M. Bat-Erdene, M. J. Biggs and J. G. Shapter, *ACS Appl. Mater. Interfaces*, 2017, **9**, 19945–19954.

165 Y. Bai, Q. Dong, Y. Shao, Y. Deng, Q. Wang, L. Shen, D. Wang, W. Wei and J. Huang, *Nat. Commun.*, 2016, **7**, 12806.

166 C. Tian, K. Kochiss, E. Castro, G. Betancourt-Solis, H. Han and L. Echegoyen, *J. Mater. Chem. A*, 2017, **5**, 7326–7332.

167 E. Bi, H. Chen, F. Xie, Y. Wu, W. Chen, Y. Su, A. Islam, M. Grätzel, X. Yang and L. Han, *Nat. Commun.*, 2017, **8**, 15330.

168 T. Mahmoudi, Y. Wang and Y.-B. Hahn, *Adv. Energy Mater.*, 2020, **10**, 1903369.

169 C. Tian, E. Castro, G. Betancourt-Solis, Z. Nan, O. Fernandez-Delgado, S. Jankuru and L. Echegoyen, *New J. Chem.*, 2018, **42**, 2896–2902.

170 C. Kuang, G. Tang, T. Jiu, H. Yang, H. Liu, B. Li, W. Luo, X. Li, W. Zhang, F. Lu, J. Fang and Y. Li, *Nano Lett.*, 2015, **15**, 2756–2762.

171 G. Namkoong, A. A. Mamun and T. T. Ava, *Org. Electron.*, 2018, **56**, 163–169.

172 J.-P. Correa-Baena, M. Anaya, G. Lozano, W. Tress, K. Domanski, M. Saliba, T. Matsui, T. J. Jacobsson, M. E. Calvo, A. Abate, M. Grätzel, H. Míguez and A. Hagfeldt, *Adv. Mater.*, 2016, **28**, 5031–5037.

173 Q. Guo, F. Yuan, B. Zhang, S. Zhou, J. Zhang, Y. Bai, L. Fan, T. Hayat, A. Alsaedi and Z. A. Tan, *Nanoscale*, 2019, **11**, 115–124.

174 M. Yavari, M. Mazloum-Ardakani, S. Gholipour, N. Marinova, J. L. Delgado, S.-H. Turren-Cruz, K. Domanski, N. Taghavinia, M. Saliba, M. Grätzel, A. Hagfeldt and W. Tress, *Adv. Energy Mater.*, 2018, **8**, 1702719.

175 B. Chen, P. N. Rudd, S. Yang, Y. Yuan and J. Huang, *Chem. Soc. Rev.*, 2019, **48**, 3842–3867.

176 J. Zhu, B. He, Z. Gong, Y. Ding, W. Zhang, X. Li, Z. Zong, H. Chen and Q. Tang, *ChemSusChem*, 2020, **13**, 1–11, DOI: 10.1002/cssc.201903288.

177 Y. Wen, G. Zhu and Y. Shao, *J. Mater. Sci.*, 2020, **55**, 2937–2946.

178 X. Gan, S. Yang, J. Zhang, G. Wang, P. He, H. Sun, H. Yuan, L. Yu, G. Ding and Y. Zhu, *ACS Appl. Mater. Interfaces*, 2019, **11**, 37796–37803.

179 C. Wu, K. Wang, Y. Yan, D. Yang, Y. Jiang, B. Chi, J. Liu, A. R. Esker, J. Rowe, A. J. Morris, M. Sanghadasa and S. Priya, *Adv. Funct. Mater.*, 2019, **29**, 1804419.

180 J. V. Milić, N. Arora, M. I. Dar, S. M. Zakeeruddin and M. Grätzel, *Adv. Mater. Interfaces*, 2018, **5**, 1800416.

181 S.-S. Li, K.-H. Tu, C.-C. Lin, C.-W. Chen and M. Chhowalla, *ACS Nano*, 2010, **4**, 3169–3174.

182 J.-M. Yun, J.-S. Yeo, J. Kim, H.-G. Jeong, D.-Y. Kim, Y.-J. Noh, S.-S. Kim, B.-C. Ku and S.-I. Na, *Adv. Mater.*, 2011, **23**, 4923–4928.

183 M. Cai, V. T. Tiong, T. Hreid, J. Bell and H. Wang, *J. Mater. Chem. A*, 2015, **3**, 2784–2793.

184 C. Rodríguez-Seco, L. Cabau, A. Vidal-Ferran and E. Palomares, *Acc. Chem. Res.*, 2018, **51**, 869–880.

185 A. K. Jena, Y. Numata, M. Ikegami and T. Miyasaka, *J. Mater. Chem. A*, 2018, **6**, 2219–2230.

186 K. Domanski, J.-P. Correa-Baena, N. Mine, M. K. Nazeeruddin, A. Abate, M. Saliba, W. Tress, A. Hagfeldt and M. Grätzel, *ACS Nano*, 2016, **10**, 6306–6314.

187 J. Zhang, T. Zhang, L. Jiang, U. Bach and Y.-B. Cheng, *ACS Energy Lett.*, 2018, **3**, 1677–1682.

188 A. L. Palma, L. Cinà, S. Pescetelli, A. Agresti, M. Raggio, R. Paolesse, F. Bonaccorso and A. Di Carlo, *Nano Energy*, 2016, **22**, 349–360.

189 B. Xu, S.-A. Gopalan, A.-I. Gopalan, N. Muthuchamy, K.-P. Lee, J.-S. Lee, Y. Jiang, S.-W. Lee, S.-W. Kim, J.-S. Kim, H.-M. Jeong, J.-B. Kwon, J.-H. Bae and S.-W. Kang, *Sci. Rep.*, 2017, **7**, 45079.

190 R. Zhang, Y. Chen, J. Xiong and X. Liu, *J. Mater. Sci.*, 2018, **53**, 4507–4514.

191 E. Nouri, M. R. Mohammadi and P. Lianos, *Carbon*, 2018, **126**, 208–214.

192 T. Miletić, E. Pavoni, V. Trifiletti, A. Rizzo, A. Listorti, S. Colella, N. Armaroli and D. Bonifazi, *ACS Appl. Mater. Interfaces*, 2016, **8**, 27966–27973.

193 W. Chen, Y. Wu, J. Fan, A. B. Djurišić, F. Liu, H. W. Tam, A. Ng, C. Surya, W. K. Chan, D. Wang and Z.-B. He, *Adv. Energy Mater.*, 2018, **8**, 1703519.

194 Z. Wang, X. Rong, L. Wang, W. Wang, H. Lin and X. Li, *ACS Appl. Mater. Interfaces*, 2020, **12**, 8342–8350.

195 J. Cao, Y.-M. Liu, X. Jing, J. Yin, J. Li, B. Xu, Y.-Z. Tan and N. Zheng, *J. Am. Chem. Soc.*, 2015, **137**, 10914–10917.

196 R. Ishikawa, S. Watanabe, S. Yamazaki, T. Oya and N. Tsuboi, *ACS Appl. Energy Mater.*, 2019, **2**, 171–175.

197 M. O. Reese, S. A. Gevorgyan, M. Jørgensen, E. Bundgaard, S. R. Kurtz, D. S. Ginley, D. C. Olson, M. T. Lloyd, P. Morvillo, E. A. Katz, A. Elschner, O. Haillant, T. R. Currier, V. Shrotriya, M. Hermenau, M. Riede, K. R. Kirov, G. Trimmel, T. Rath, O. Inganäs, F. Zhang, M. Andersson, K. Tvingstedt, M. Lira-Cantu, D. Laird, C. McGuiness, S. Gowrisanker, M. Pannone, M. Xiao, J. Hauch, R. Steim, D. M. DeLongchamp, R. Rösch, H. Hoppe, N. Espinosa, A. Urbina, G. Yaman-Uzunoglu, J.-B. Bonekamp, A. J. J. M. van Breemen, C. Girotto, E. Voroshazi and F. C. Krebs, *Sol. Energy Mater. Sol. Cells*, 2011, **95**, 1253–1267.

198 A. Guerrero, J. You, C. Aranda, Y. S. Kang, G. Garcia-Belmonte, H. Zhou, J. Bisquert and Y. Yang, *ACS Nano*, 2016, **10**, 218–224.

199 A. K. Baranwal, S. Kanaya, T. A. N. Peiris, G. Mizuta, T. Nishina, H. Kanda, T. Miyasaka, H. Segawa and S. Ito, *ChemSusChem*, 2016, **9**, 2604–2608.

200 F. Zhang, X. Yang, M. Cheng, W. Wang and L. Sun, *Nano Energy*, 2016, **20**, 108–116.

201 K. Cao, Z. Zuo, J. Cui, Y. Shen, T. Moehl, S. M. Zakeeruddin, M. Grätzel and M. Wang, *Nano Energy*, 2015, **17**, 171–179.

202 N. Zhang, Y. Guo, X. Yin, M. He and X. Zou, *Mater. Lett.*, 2016, **182**, 248–252.

203 K. Aitola, K. Domanski, J.-P. Correa-Baena, K. Sveinbjörnsson, M. Saliba, A. Abate, M. Grätzel, E. Kauppinen, E. M. J. Johansson, W. Tress, A. Hagfeldt and G. Boschloo, *Adv. Mater.*, 2017, **29**, 1606398.

204 F. Meng, L. Gao, Y. Yan, J. Cao, N. Wang, T. Wang and T. Ma, *Carbon*, 2019, **145**, 290–296.

205 S. Gholipour, J.-P. Correa-Baena, K. Domanski, T. Matsui, L. Steier, F. Giordano, F. Tajabadi, W. Tress, M. Saliba, A. Abate, A. Morteza Ali, N. Taghavinia, M. Grätzel and A. Hagfeldt, *Adv. Energy Mater.*, 2016, **6**, 1601116.

206 X. Xu, Z. Liu, Z. Zuo, M. Zhang, Z. Zhao, Y. Shen, H. Zhou, Q. Chen, Y. Yang and M. Wang, *Nano Lett.*, 2015, **15**, 2402–2408.

207 R. Dileep, G. Kesavan, V. Reddy, M. K. Rajbhar, S. Shanmugasundaram, E. Ramasamy and G. Veerappan, *Sol. Energy*, 2019, **187**, 261–268.

208 Y. Zhang, X. Zhuang, K. Zhou, C. Cai, Z. Hu, J. Zhang and Y. Zhu, *Org. Electron.*, 2018, **52**, 159–164.

209 S. G. Hashmi, D. Martineau, M. I. Dar, T. T. T. Myllymäki, T. Sarikka, V. Ulla, S. M. Zakeeruddin and M. Grätzel, *J. Mater. Chem. A*, 2017, **5**, 12060–12067.

210 Z. Yu, B. Chen, P. Liu, C. Wang, C. Bu, N. Cheng, S. Bai, Y. Yan and X. Zhao, *Adv. Funct. Mater.*, 2016, **26**, 4866–4873.

211 J. Ryu, K. Lee, J. Yun, H. Yu, J. Lee and J. Jang, *Small*, 2017, **13**, 1701225.

212 X. Li, M. Tschumi, H. Han, S. S. Babkair, R. A. Alzubaydi, A. A. Ansari, S. S. Habib, M. K. Nazeeruddin, S. M. Zakeeruddin and M. Grätzel, *Energy Technol.*, 2015, **3**, 551–555.

213 Z. Wei, H. Chen, K. Yan and S. Yang, *Angew. Chem., Int. Ed.*, 2014, **126**, 13455–13459.

214 F. Zhang, X. Yang, H. Wang, M. Cheng, J. Zhao and L. Sun, *ACS Appl. Mater. Interfaces*, 2014, **6**, 16140–16146.

215 H. Wei, J. Xiao, Y. Yang, S. Lv, J. Shi, X. Xu, J. Dong, Y. Luo, D. Li and Q. Meng, *Carbon*, 2015, **93**, 861–868.

216 H. Zhou, Y. Shi, K. Wang, Q. Dong, X. Bai, Y. Xing, Y. Du and T. Ma, *J. Phys. Chem. C*, 2015, **119**, 4600–4605.

217 Z. Liu, B. Sun, T. Shi, Z. Tang and G. Liao, *J. Mater. Chem. A*, 2016, **4**, 10700–10709.

218 C.-Y. Chan, Y. Wang, G.-W. Wu and E. Wei-Guang Diau, *J. Mater. Chem. A*, 2016, **4**, 3872–3878.

219 Z. Liu, T. Shi, Z. Tang, B. Sun and G. Liao, *Nanoscale*, 2016, **8**, 7017–7023.

220 G. Yue, D. Chen, P. Wang, J. Zhang, Z. Hu and Y. Zhu, *Electrochim. Acta*, 2016, **218**, 84–90.

221 C. Zhang, Y. Luo, X. Chen, Y. Chen, Z. Sun and S. Huang, *Nano-Micro Letters*, 2016, **8**, 347–357.

222 C.-M. Tsai, G.-W. Wu, S. Narra, H.-M. Chang, N. Mohanta, H.-P. Wu, C.-L. Wang and E. W.-G. Diau, *J. Mater. Chem. A*, 2017, **5**, 739–747.

223 S. G. Hashmi, D. Martineau, X. Li, M. Ozkan, A. Tiihonen, M. I. Dar, T. Sarikka, S. M. Zakeeruddin, J. Paltakari, P. D. Lund and M. Grätzel, *Adv. Mater. Technol.*, 2017, **2**, 1600183.

224 L. Xu, F. Wan, Y. Rong, H. Chen, S. He, X. Xu, G. Liu, H. Han, Y. Yuan, J. Yang, Y. Gao, B. Yang and C. Zhou, *Org. Electron.*, 2017, **45**, 131–138.

225 M. Chen, R.-H. Zha, Z.-Y. Yuan, Q.-S. Jing, Z.-Y. Huang, X.-K. Yang, S.-M. Yang, X.-H. Zhao, D.-L. Xu and G.-D. Zou, *Chem. Eng. J.*, 2017, **313**, 791–800.

226 G. Grancini, C. Roldán-Carmona, I. Zimmermann, E. Mosconi, X. Lee, D. Martineau, S. Narbey, F. Oswald, F. De Angelis, M. Graetzel and M. K. Nazeeruddin, *Nat. Commun.*, 2017, **8**, 15684.

227 X. Chang, W. Li, L. Zhu, H. Liu, H. Geng, S. Xiang, J. Liu and H. Chen, *ACS Appl. Mater. Interfaces*, 2016, **8**, 33649–33655.

228 J. Li, J. X. Yao, X. Y. Liao, R. L. Yu, H. R. Xia, W. T. Sun and L. M. Peng, *RSC Adv.*, 2017, **7**, 20732–20737.

229 K. Cao, J. Cui, H. Zhang, H. Li, J. Song, Y. Shen, Y. Cheng and M. Wang, *J. Mater. Chem. A*, 2015, **3**, 9116–9122.

230 Q. Luo, H. Ma, Y. Zhang, X. Yin, Z. Yao, N. Wang, J. Li, S. Fan, K. Jiang and H. Lin, *J. Mater. Chem. A*, 2016, **4**, 5569–5577.

231 S. Xiang, W. Li, Y. Wei, J. Liu, H. Liu, L. Zhu, S. Yang and H. Chen, *iScience*, 2019, **15**, 156–164.

232 X. Zheng, H. Chen, Q. Li, Y. Yang, Z. Wei, Y. Bai, Y. Qiu, D. Zhou, K. S. Wong and S. Yang, *Nano Lett.*, 2017, **17**, 2496–2505.

233 B. Zong, W. Fu, Z.-a. Guo, S. Wang, L. Huang, B. Zhang, H. Bala, J. Cao, X. Wang, G. Sun and Z. Zhang, *J. Colloid Interface Sci.*, 2019, **540**, 315–321.

234 X. Zhang, Y. Zhou, Y. Li, J. Sun, X. Lu, X. Gao, J. Gao, L. Shui, S. Wu and J.-M. Liu, *J. Mater. Chem. C*, 2019, **7**, 3852–3861.

235 Y. Yang, Z. Liu, W. K. Ng, L. Zhang, H. Zhang, X. Meng, Y. Bai, S. Xiao, T. Zhang, C. Hu, K. S. Wong and S. Yang, *Adv. Funct. Mater.*, 2019, **29**, 1806506.

236 P. Liu, Y. Gong, Y. Xiao, M. Su, S. Kong, F. Qi, H. Zhang, S. Wang, X. Sun, C. Wang and X.-Z. Zhao, *Chem. Commun.*, 2019, **55**, 218–221.
237 S. Wang, H. Liu, H. Bala, B. Zong, L. Huang, Z.-a. Guo, W. Fu, B. Zhang, G. Sun, J. Cao and Z. Zhang, *Electrochim. Acta*, 2020, **335**, 135686.
238 F. Meng, A. Liu, L. Gao, J. Cao, Y. Yan, N. Wang, M. Fan, G. Wei and T. Ma, *J. Mater. Chem. A*, 2019, **7**, 8690–8699.
239 Z. Wei, X. Zheng, H. Chen, X. Long, Z. Wang and S. Yang, *J. Mater. Chem. A*, 2015, **3**, 16430–16434.
240 I. K. Popoola, M. A. Gondal and T. F. Qahtan, *Renewable Sustainable Energy Rev.*, 2018, **82**, 3127–3151.
241 K. Cui and S. Maruyama, *Prog. Energy Combust. Sci.*, 2019, **70**, 1–21.
242 F. El-Mellouhi, A. Marzouk, E. T. Bentria, S. N. Rashkeev, S. Kais and F. H. Alharbi, *ChemSusChem*, 2016, **9**, 2648–2655.
243 S. Kim, S. Bae, S.-W. Lee, K. Cho, K. D. Lee, H. Kim, S. Park, G. Kwon, S.-W. Ahn, H.-M. Lee, Y. Kang, H.-S. Lee and D. Kim, *Sci. Rep.*, 2017, **7**, 1200.
244 Y. Zhao, W. Zhou, H. Tan, R. Fu, Q. Li, F. Lin, D. Yu, G. Walters, E. H. Sargent and Q. Zhao, *J. Phys. Chem. C*, 2017, **121**, 14517–14523.
245 Y. Song, W. Bi, A. Wang, X. Liu, Y. Kang and Q. Dong, *Nat. Commun.*, 2020, **11**, 274.
246 J. Lee, S. Singh, S. Kim and S. Baik, *Carbon*, 2020, **157**, 731–740.
247 S. Guarnera, A. Abate, W. Zhang, J. M. Foster, G. Richardson, A. Petrozza and H. J. Snaith, *J. Phys. Chem. Lett.*, 2015, **6**, 432–437.
248 F. Pan, C. Sun, Y. Li, D. Tang, Y. Zou, X. Li, S. Bai, X. Wei, M. Lv, X. Chen and Y. Li, *Energy Environ. Sci.*, 2019, **12**, 3400–3411.
249 T. Leijtens, G. E. Eperon, S. Pathak, A. Abate, M. M. Lee and H. J. Snaith, *Nat. Commun.*, 2013, **4**, 2885.
250 M. A. Mahmud, N. K. Elumalai, M. B. Upama, D. Wang, L. Zarei, V. R. Gonçales, M. Wright, C. Xu, F. Haque and A. Uddin, *Nanoscale*, 2018, **10**, 773–790.
251 N. Ahn, I. Jeon, J. Yoon, E. I. Kauppinen, Y. Matsuo, S. Maruyama and M. Choi, *J. Mater. Chem. A*, 2018, **6**, 1382–1389.
252 Q. Luo, H. Ma, Q. Hou, Y. Li, J. Ren, X. Dai, Z. Yao, Y. Zhou, L. Xiang, H. Du, H. He, N. Wang, K. Jiang, H. Lin, H. Zhang and Z. Guo, *Adv. Funct. Mater.*, 2018, **28**, 1706777.
253 F. Wu, W. Gao, H. Yu, L. Zhu, L. Li and C. Yang, *J. Mater. Chem. A*, 2018, **6**, 4443–4448.
254 H. Choi, J. Lee, C.-M. Oh, S. Jang, H. Kim, M. S. Jeong, S. H. Park and I.-W. Hwang, *J. Mater. Chem. A*, 2019, **7**, 8805–8810.
255 M. Acik and S. B. Darling, *J. Mater. Chem. A*, 2016, **4**, 6185–6235.
256 S. S. Mali, J. V. Patil and C. K. Hong, *J. Mater. Chem. A*, 2019, **7**, 10246–10255.
257 T. A. Berhe, W.-N. Su, C.-H. Chen, C.-J. Pan, J.-H. Cheng, H.-M. Chen, M.-C. Tsai, L.-Y. Chen, A. A. Dubale and B.-J. Hwang, *Energy Environ. Sci.*, 2016, **9**, 323–356.
258 L. Meng, J. You and Y. Yang, *Nat. Commun.*, 2018, **9**, 5265.
259 G. Divitini, S. Cacovich, F. Matteocci, L. Cinà, A. Di Carlo and C. Ducati, *Nat. Energy*, 2016, **1**, 15012.
260 B. Conings, J. Drijkoningen, N. Gauquelin, A. Babayigit, J. D'Haen, L. D'Olieslaeger, A. Ethirajan, J. Verbeeck, J. Manca, E. Mosconi, F. D. Angelis and H.-G. Boyen, *Adv. Energy Mater.*, 2015, **5**, 1500477.
261 J.-A. Alberola-Borràs, J. A. Baker, F. De Rossi, R. Vidal, D. Beynon, K. E. A. Hooper, T. M. Watson and I. Mora-Seró, *iScience*, 2018, **9**, 542–551.
262 Y. Jiang, M. R. Leyden, L. Qiu, S. Wang, L. K. Ono, Z. Wu, E. J. Juarez-Perez and Y. Qi, *Adv. Funct. Mater.*, 2018, **28**, 1703835.
263 J. Baker, K. Hooper, S. Meroni, A. Pockett, J. McGettrick, Z. Wei, R. Escalante, G. Oskam, M. Carnie and T. Watson, *J. Mater. Chem. A*, 2017, **5**, 18643–18650.
264 A. Priyadarshi, L. J. Haur, P. Murray, D. Fu, S. Kulkarni, G. Xing, T. C. Sum, N. Mathews and S. G. Mhaisalkar, *Energy Environ. Sci.*, 2016, **9**, 3687–3692.
265 Y. Hu, S. Si, A. Mei, Y. Rong, H. Liu, X. Li and H. Han, *Sol. RRL*, 2017, **1**, 1600019.